Research Square

Preprints are preliminary reports that have not undergone peer review.
They should not be considered conclusive, used to inform clinical practice,
or referenced by the media as validated information.

Organoid-Derived β-Catenin-Overexpressing Dendritic Cells Alleviate Sepsis- Induced Acute Lung Injury

Di Wang
Department of Critical Care Medicine, The First Affiliated Hospital of USTC, Division of Life Sciences and Medicine, University of Science and Technology of China

Xiaojing Chen
Department of Endocrinology, Xinhua Hospital, Shanghai Jiao Tong University School of Medicine

Jie Shan
Department of Burns, The First Affiliated Hospital of Anhui Medical University

Tianfeng Wang
Department of Critical Care Medicine, The First Affiliated Hospital of USTC, Division of Life Sciences and Medicine, University of Science and Technology of China

Leiting Shen
Department of Critical Care Medicine, The First Affiliated Hospital of USTC, Division of Life Sciences and Medicine, University of Science and Technology of China

Fan Xu
Department of Critical Care Medicine, The First Affiliated Hospital of USTC, Division of Life Sciences and Medicine, University of Science and Technology of China

Qian Wang
Department of Critical Care Medicine, The First Affiliated Hospital of USTC, Division of Life Sciences and Medicine, University of Science and Technology of China

Xiaowei Fang
Department of Critical Care Medicine, The First Affiliated Hospital of USTC, Division of Life Sciences and Medicine, University of Science and Technology of China

Qing Mei
Department of Critical Care Medicine, The First Affiliated Hospital of USTC, Division of Life Sciences and Medicine, University of Science and Technology of China

Yuqing Zhu
Center for Stem Cell and Translational Medicine, School of Life Sciences, Anhui University

Shoudong Ye
Center for Stem Cell and Translational Medicine, School of Life Sciences, Anhui University

Min Zhou

dminzhou@ustc.edu.cn

Department of Critical Care Medicine, The First Affiliated Hospital of USTC, Division of Life Sciences and Medicine, University of Science and Technology of China

---

Research Article

Keywords: Vascular-hematopoietic organoids, Wnt/β-catenin signaling, Hematopoietic differentiation, genetically engineered dendritic cells, T-cell activation, Sepsis-induced acute lung injury

Posted Date: September 8th, 2026

DOI: https://doi.org/10.21203/rs.3.rs-10828161/v1

License: This work is licensed under a Creative Commons Attribution 4.0 International License. Read Full License

Additional Declarations: No competing interests reported.

Organoid-Derived β-Catenin-Overexpressing Dendritic Cells Alleviate Sepsis-Induced Acute Lung Injury

Di Wang[1,#], Xiaojing Chen[2,#], Jie Shan[4,#], Tianfeng Wang[1], Leiting Shen[1], Fan Xu[1], Qian Wang[1], Xiaowei Fang[1], Qing Mei[1], Yuqing Zhu[3,*], Shoudong Ye[3,*] and Min Zhou[1,*]

[#]Di Wang, Xiaojing Chen, and Jie Shan contributed equally to this work.

[1]Department of Critical Care Medicine, The First Affiliated Hospital of USTC, Division of Life Sciences and Medicine, University of Science and Technology of China, Hefei, Anhui Province, 230001, China

[2]Department of Endocrinology, Xinhua Hospital, Shanghai Jiao Tong University School of Medicine, Shanghai 200092, China

[3]Center for Stem Cell and Translational Medicine, School of Life Sciences, Anhui University, Hefei, Anhui Province, 230001, China

[4]Department of Burns, The First Affiliated Hospital of Anhui Medical University, Hefei, Anhui Province, 230001, China

*Correspondence: Min Zhou (dminzhou@ustc.edu.cn); Shoudong Ye (shdye@126.com); Yuqing Zhu (zhuyuqingccnu@126.com).

Abstract

Background

Sepsis-induced acute lung injury (ALI) is characterized by pulmonary immune dysregulation, while the limited availability and functional stability of conventional dendritic cells (DCs) constrain their therapeutic application. We investigated whether β-catenin engineering at the mouse embryonic stem cell (mESC) stage could enhance blood vessel organoid (BVO)-based DC generation and improve DC-mediated immune regulation in sepsis-induced ALI.

Methods

β-Catenin-overexpressing (β-cat^{OE}) mESCs were sequentially differentiated through a

three-dimensional BVO–hematopoietic progenitor–DC pipeline. Hematopoietic differentiation, DC phenotype and function, ovalbumin (OVA)-containing OT-II/OT-I T-cell responses, and transcriptomic profiles were evaluated. Therapeutic effects were assessed following intranasal administration of β-cat^{OE} BVO-derived DCs (BVO-DCs) in a cecal ligation and puncture (CLP)-induced sepsis model by pulmonary bioluminescence imaging, lung injury and inflammation assessment, pulmonary T-cell analysis, and 96-h survival monitoring. Statistical comparisons were performed using t-tests or analysis of variance as appropriate, with survival analyzed by the log-rank test.

Results

β-Catenin overexpression increased hematopoietic progenitor frequency to 11.96 ± 1.55% and total cell yield to (12.52 ± 1.43) × 10^7 cells. Following lipopolysaccharide stimulation, β-cat^{OE} BVO-DCs showed 47.73 ± 7.77% major histocompatibility complex class II (MHC-II) positivity and induced CD40 ligand (CD40L) expression in OT-II $CD4^+$ T cells (35.37 ± 3.45%), OT-I $CD8^+$ T-cell proliferation (77.01 ± 7.46%), and CD25 expression (51.84 ± 4.61%) in full-length OVA-containing co-cultures. Blockade experiments supported the involvement of the MHC-II/$CD4^+$ T-cell/CD40L axis. Transcriptomic analysis showed enhanced Wnt signaling, DC differentiation, and MHC-mediated antigen-presentation programs. In CLP-induced sepsis, β-cat^{OE} BVO-DC treatment increased pulmonary bioluminescence at 24 and 48 h, attenuated lung injury and inflammatory responses, and improved 96-h survival to 53.3% compared with 13.3% in untreated CLP mice. Treatment also increased pulmonary $CD8^+$ T-cell abundance and reduced the bronchoalveolar lavage fluid (BALF) $CD4^+/CD8^+$ ratio to 2.12 ± 0.40 versus 4.01 ± 0.69 in untreated CLP mice.

Conclusions

β-Catenin engineering at the mESC stage enhances hematopoietic output from BVOs and generates functionally enhanced BVO-derived DCs that improve pulmonary immune balance and outcomes in experimental sepsis-induced ALI. These findings support further development of organoid-based DC strategies for sepsis-associated immunosuppression.

Keywords: Vascular-hematopoietic organoids**,** Wnt/β-catenin signaling, Hematopoietic differentiation, genetically engineered dendritic cells, T-cell activation,

Sepsis-induced acute lung injury.

Background

Sepsis remains a leading cause of mortality in intensive care units globally, with the lung serving as the earliest and most vulnerable target organ, frequently manifesting as acute lung injury (ALI) [1, 2]. Sepsis-induced ALI is driven by a complex interplay between excessive inflammation and profound immune dysfunction [3]. Conventional therapies have historically targeted the early hyperinflammatory cytokine storm, whereas emerging evidence indicates that the progression of sepsis-induced ALI is largely driven by localized immune paralysis [4]. Crucially, multicenter clinical data indicate that severe pulmonary infection is accompanied by selective $CD8^+$ T-cell depletion and $CD4^+/CD8^+$ T-cell imbalance, with an elevated $CD4^+/CD8^+$ ratio associated with increased 28-day mortality [5, 6]. This disruption of adaptive immune homeostasis compromises pulmonary immune defense, increasing susceptibility to secondary infections and impaired tissue repair [7]. Consequently, strategies aimed at restoring pulmonary adaptive immune competence and reversing T-cell dysfunction represent a promising therapeutic avenue for sepsis-induced ALI.

As antigen-presenting cells, dendritic cells (DCs) possess the unique capacity to prime $CD4^+$ T-helper cells, which subsequently facilitate the activation and robust proliferation of cytotoxic $CD8^+$ T-cells to counteract localized immune paralysis [8]. By restoring this immunological balance, DC cellular therapy represents a promising avenue for reactivating exhausted T-cells [9]. However, conventional bone marrow-derived DCs (BM-DCs) or peripheral blood monocyte-derived DCs face formidable bottlenecks during in vitro preparation, often suffering from cellular functional exhaustion and substantial batch-to-batch heterogeneity after prolonged culture [8]. Furthermore, these conventional platforms are restricted by technical manufacturing hurdles such as low antigen-loading efficiency, and without specialized microenvironmental support, they frequently undergo functional inactivation upon exposure to complex, suppressive in vivo microenvironments [10].

To address these constraints, embryonic stem cell (ESC)-derived organoids have emerged as powerful three-dimensional (3D) platforms for investigating lineage specification and tissue morphogenesis. On one hand, ESCs provide unique advantages,

including an essentially unlimited cellular source through long-term expansion and the flexibility for clustered regularly interspaced short palindromic repeats/CRISPR-associated protein (CRISPR/Cas)-mediated site-specific genome engineering [11]. These genetic engineering capabilities enable a single starting cell population to differentiate into multiple specialized lineages under defined regulatory programs, thereby reducing donor heterogeneity and facilitating the development of efficient, scalable, and reproducible organoid production platforms [12]. On the other hand, unlike conventional two-dimensional (2D) monolayer cultures that are often limited by inadequate microenvironmental cues, 3D organoid systems better recapitulate tissue complexity by reconstructing multiscale structural organization and promoting intricate cell–cell interactions [13].

The canonical Wnt/β-catenin signaling pathway serves as a foundational driver that orchestrates early embryonic hematopoiesis and downstream lineage specification [14, 15]. Beyond its established roles in development and tissue homeostasis, the Wnt/β-catenin pathway has emerged as an important regulator of immune responses during severe infection [16]. Dysregulated Wnt/β-catenin signaling has been closely associated with sepsis progression, influencing inflammatory responses and cytokine production during systemic infection [17]. Recent studies have further shown that Wnt/β-catenin signaling shapes DC-mediated adaptive immunity by modulating $CD4^+$ T-cell polarization and $CD8^+$ T-cell activation [18–20], suggesting that modulation of this pathway may provide a strategy to enhance DC-mediated immune regulation during sepsis-associated immunosuppression.

Despite the recognized role of Wnt/β-catenin signaling in hematopoietic and immune regulation, it remains unclear whether β-catenin overexpression at the mouse embryonic stem cell (mESC) stage can influence hematopoietic development during blood vessel organoid (BVO) induction and thereby developmentally program BVO-derived DCs to acquire enhanced immunological functions. Moreover, whether these developmentally programmed DCs can ameliorate sepsis-induced ALI by restoring pulmonary adaptive immune homeostasis remains unknown.

Here, we developed a strategy to generate functionally enhanced DCs from β-catenin-overexpressing mESCs through BVO-based hematopoietic induction and subsequent DC differentiation. We hypothesized that β-catenin-mediated

developmental programming would enhance the antigen-presenting capacity of BVO-derived DCs, strengthen $CD4^+$ T-cell-dependent $CD8^+$ T-cell activation, and counteract the exhaustion-associated pulmonary immune dysfunction induced by sepsis, thereby restoring local T-cell homeostasis and improving outcomes in cecal ligation and puncture (CLP)-induced ALI. This study establishes a scalable developmental engineering platform for immune cell therapy and provides a potential strategy for sepsis immunomodulation.

Methods

Cell Line Cultivation and Lentiviral Genetic Engineering

The 46C mouse embryonic stem cell (mESC) line, maintained as an in-house laboratory stock (Additional file 1: Table S1), was cultured on 0.1% gelatin-coated plates in complete mESC medium comprising high-glucose Dulbecco's modified Eagle medium (DMEM), 10% defined fetal bovine serum (FBS), 1000 U/mL mouse leukemia inhibitory factor (LIF), the 2i inhibitors CHIR-99021 (3 μM) and PD0325901 (1 μM), 0.1 mM β-mercaptoethanol, 2 mM GlutaMAX, 0.1 mM MEM non-essential amino acids (NEAA), 50 U/mL penicillin, and 50 μg/mL streptomycin (Additional file 1: Table S2).

To generate stable β-catenin-overexpressing mESCs, cells were transduced with a pLV4ltr-PGK-ZsGreen(2A)-Puro-CMV lentiviral vector encoding full-length mouse Ctnnb1. A corresponding empty vector lacking Ctnnb1 but retaining the ZsGreen reporter and puromycin-resistance cassette was used to generate the empty-vector (EV) control mESCs (Additional file 1: Table S1). mESCs were transduced at a multiplicity of infection (MOI) of 20 in the presence of 8 μg/mL polybrene and selected with 2 μg/mL puromycin for 7 days. ZsGreen fluorescence was used to monitor transduction, and the resulting antibiotic-selected stable cell populations were designated EV mESCs and β-cat^{OE} mESCs. β-catenin overexpression was verified by reverse-transcription quantitative PCR (RT-qPCR) and Western blotting. The expression of the pluripotency-associated genes Nanog, Pou5f1 (Oct4), and Sox2 was evaluated by RT-qPCR, and the corresponding proteins were assessed by immunofluorescence staining (Additional file 1: Tables S1, S3, and S4). For cell-tracking experiments, EV and β-cat^{OE} mESCs were additionally transduced with the pLV-LucGFP-Luciferase-Neo^R lentiviral vector and

selected with Geneticin/G418 at 350 μg/mL for 2 days, followed by 150 μg/mL for an additional 3–5 days, generating Luc-EV and Luc-β-cat^{OE} mESCs, respectively (Additional file 1: Tables S1 and S2).

Characterization of the Hematopoietic Differentiation Potential of 3D BVOs

Mouse BVOs were generated using a previously established sequential cytokine-guided induction protocol [21]. Each induction batch was initiated with 5×10^5 single mESCs. Cells were aggregated into embryoid bodies (EBs) in N2B27 medium prepared from Neurobasal and DMEM/F12 media supplemented with N2 and B27 (Additional file 1: Table S2). The medium was further supplemented with 3 μM CHIR-99021 and 10 ng/mL bone morphogenetic protein 4 (BMP4). Cells were seeded into U-bottom ultra-low-attachment 96-well plates at 3,000 cells in 100 μL per well and incubated for 48 h. On Day 2, the EBs were transferred to hematoendothelial specification medium containing BMP4 (10 ng/mL), vascular endothelial growth factor (VEGF) (50 ng/mL), basic fibroblast growth factor (bFGF) (10 ng/mL), and stem cell factor (SCF) (50 ng/mL).

On Day 5, uniformly sized EBs were embedded in a 3D matrix comprising PureCol® bovine type I atelocollagen solution (3 mg/mL) and growth-factor-reduced, phenol red-free, LDEV-free Corning® Matrigel® at a 3:1 (v/v) ratio and cultured in 12-well plates at 10 EBs per well (Additional file 1: Table S2). Hematopoietic specification was performed using a two-stage induction strategy. During Phase I (Days 5–8), vascular sprouting was promoted using vascular–hematopoietic expansion medium supplemented with VEGF (100 ng/mL), bFGF (20 ng/mL), SCF (100 ng/mL), and Fms-like tyrosine kinase 3 ligand (Flt3L) (10 ng/mL). During Phase II (Days 8–11), half of the culture medium was replaced, and the cytokine concentrations were adjusted to final concentrations of VEGF (100 ng/mL), bFGF (20 ng/mL), SCF (100 ng/mL), Flt3L (10 ng/mL), IL-6 (10 ng/mL), IL-3 (10 ng/mL), and thrombopoietin (TPO) (10 ng/mL) to support vascular maturation and hematopoietic emergence.

BVO morphology was monitored by phase-contrast microscopy on Days 0, 2, 5, 8, and 11 using a Leica DMi8 inverted microscope (Additional file 1: Table S5), documenting EB formation, endothelial sprouting, vascular-like organization, and hematopoietic-like cell emergence. For whole-mount imaging, Day 8 BVOs were fixed in 4% paraformaldehyde, permeabilized, and blocked before incubation with antibodies

against CD31 and PDGFR-β or collagen IV and PDGFR-β. After staining with the appropriate fluorescent secondary antibodies and DAPI (Additional file 1: Tables S1 and S3), whole-mount BVOs were optically cleared with Corning 3D Clear tissue clearing reagent according to the manufacturer's instructions and subsequently imaged using an ImageXpress Micro Confocal High-Content Imaging System (Molecular Devices) under identical acquisition settings.

Separate BVO batches were harvested on Days 8 and 11 for multiparameter flow cytometric analysis of vascular and hematopoietic populations using antibodies against Flk-1, VE-cadherin, CD31, PDGFR-β, lineage markers (Lin), CD117, CD43, and CD45 (Additional file 1: Table S3). Cell viability was assessed using 7-aminoactinomycin D (7-AAD), with viable cells defined as the 7-AAD$^-$ population. Debris was excluded based on forward- and side-scatter characteristics, and doublets were excluded using singlet-gating parameters. For quantitative group analyses, subpopulation frequencies were expressed relative to the total 7-AAD$^-$ live-cell population, whereas frequencies in representative sequential gating plots were expressed relative to the indicated parent gates. Flow cytometric data were acquired using a Navios EX flow cytometer (Additional file 1: Table S5).

Sequential DC Differentiation and Immunomagnetic Enrichment

On Day 11, EV and β-cat^{OE} BVOs were dissociated into single-cell suspensions by sequential digestion with collagenase type I (1 mg/mL, 37 °C, 20 min) and Accutase (37 °C, 10 min). The cells were passed through a 70-μm cell strainer, and viable cell numbers were determined by trypan blue exclusion. Following Fc receptor blockade with anti-mouse CD16/CD32, CD45$^+$ hematopoietic cells were enriched by positive immunomagnetic selection using anti-mouse CD45 MicroBeads and operationally designated the committed hematopoietic progenitor cell (CHPC)-enriched fraction (Additional file 1: Tables S1 and S3).

The CHPC-enriched cells were cultured from Days 11–14 (DC differentiation Days 1–4) in early-stage DC differentiation medium comprising RPMI 1640, 10% FBS, 50 U/mL penicillin, 50 μg/mL streptomycin, mouse Flt3L (50 ng/mL), SCF (50 ng/mL), TPO (10 ng/mL), and granulocyte-macrophage colony-stimulating factor (GM-CSF) (40 ng/mL). On Day 14, non-adherent and loosely adherent cells were collected and enriched by positive immunomagnetic selection using anti-mouse CD11c MicroBeads.

The enriched cells were cultured for an additional 4 days (Days 14–18; DC differentiation Days 4–8) in late-stage DC differentiation medium comprising RPMI 1640, 10% FBS, 50 U/mL penicillin, 50 μg/mL streptomycin, 50 μM 2-mercaptoethanol, GM-CSF (40 ng/mL), and IL-4 (40 ng/mL) (Additional file 1: Tables S1 and S2). The resulting cells were designated EV BVO-DCs and β-cat^{OE} BVO-DCs.

RT-qPCR and Western Blotting

Total RNA was extracted from EV and β-cat^{OE} mESCs using TRIzol LS reagent (Additional file 1: Table S1). cDNA was synthesized using the PrimeScript RT Reagent Kit with gDNA Eraser, and quantitative PCR was performed using TB Green Premix Ex Taq II on a QuantStudio real-time PCR system (Thermo Fisher Scientific). Primer sequences are provided in Additional file 1: Table S4. Actb was used as the internal reference gene, and relative gene expression was calculated using the $2^{-}\Delta\Delta Ct$ method, with the EV group normalized to 1. EV and β-cat^{OE} mESCs, BVO-derived CHPC-enriched cells, and Day 8 BVO-DCs were lysed in precooled radioimmunoprecipitation assay (RIPA) buffer supplemented with protease inhibitors (Additional file 1: Table S1). Protein concentrations were determined using a bicinchoninic acid (BCA) assay. Equal amounts of protein (20 μg per lane) were separated on 10% SDS–PAGE gels and transferred onto 0.45-μm polyvinylidene fluoride membranes. After blocking with 5% skim milk for 4 h at room temperature, the membranes were incubated overnight at 4 °C with antibodies against β-catenin and β-actin, followed by the corresponding HRP-conjugated secondary antibodies for 2 h at room temperature (Additional file 1: Table S3). Protein bands were visualized using a Tanon 5200Multi gel imaging system and quantified using Fiji/ImageJ. β-Catenin abundance was normalized to β-actin, with the corresponding EV group set to 1. Uncropped images of all Western blots are provided in Additional file 2.

Generation of Primary BM-DCs and Isolation of OT-I/OT-II T Cells

Bone marrow cells were flushed from the femurs and tibias of wild-type C57BL/6J mice, passed through a 70-μm cell strainer, washed, and cultured for 8 days in RPMI 1640 supplemented with 10% FBS, 50 U/mL penicillin, 50 μg/mL streptomycin, 50 μM 2-mercaptoethanol, recombinant mouse GM-CSF (40 ng/mL), and recombinant mouse IL-4 (40 ng/mL). Half of the medium was replaced every 2–3 days with fresh cytokine-containing medium. On Day 8, non-adherent and loosely adherent cells were collected,

and the proportion of $CD11b^+CD11c^+$ cells within the $7\text{-}AAD^-$ live-cell population was assessed by flow cytometry. The resulting BM-DCs were used as an $H\text{-}2^b$-compatible positive control in the OT-I/OT-II co-culture assays.

OT-I and OT-II mice on a C57BL/6J background were obtained from Nanjing Zhishu Yantu Biotechnology Co., Ltd. (Additional file 1: Table S1). Splenic OT-I $CD8^+$ T cells and OT-II $CD4^+$ T cells were separately enriched by positive immunomagnetic selection using CD8α (Ly-2) and CD4 (L3T4) MicroBeads, respectively (Additional file 1: Table S1). Post-isolation purity was assessed by flow cytometry based on the frequencies of $CD8^+$ and $CD4^+$ cells within the $7\text{-}AAD^-$ live-cell population, respectively (Additional file 1: Figure S7). The OT-I T-cell receptor recognizes the $OVA_{257–264}$ epitope (SIINFEKL) presented by $H\text{-}2K^b$, whereas the OT-II T-cell receptor recognizes the $OVA_{323–339}$ epitope presented by $I\text{-}A^b$.

LPS-Induced DC Phenotypic Assessment and OVA-Containing T-Cell Activation Assays

For morphological and MHC-II phenotypic comparisons, EV BVO-DCs, primary BM-DCs, and $\beta\text{-}cat^{OE}$ BVO-DCs were cultured in the presence or absence of lipopolysaccharide derived from Escherichia coli O55:B5 (LPS; 100 ng/mL) for 48 h (Additional file 1: Table S1). After 48 h, cellular morphology under both −LPS and +LPS conditions, including adherence, spreading, clustering, and dendritic-like projections, was examined using a Leica DMi8 inverted microscope under identical image-acquisition settings (Additional file 1: Table S5). Representative phase-contrast images were acquired for qualitative comparison among the three DC populations. In parallel, cells were collected and stained with 7-AAD and antibodies against CD11b, CD11c, and MHC-II. The frequency of $MHC\text{-}II^+$ cells was quantified within the $7\text{-}AAD^-CD11b^+CD11c^+$ DC population using the upstream gating strategy shown in Additional file 1: Figure S6.

For the subsequent T-cell activation assays, LPS-stimulated DCs from all three groups were washed before co-culture. To assess OT-II $CD4^+$ T-cell activation in full-length OVA-containing co-cultures and its sensitivity to MHC-II blockade, the washed LPS-stimulated DCs were co-cultured with OT-II $CD4^+$ T cells at a DC-to-T-cell ratio of 1:10 in the presence of full-length low-endotoxin OVA (2 μg/mL) for 24 h. OT-II $CD4^+$ T cells cultured under otherwise identical conditions with OVA but without DCs

served as the baseline control. In parallel, the β-cat^{OE} BVO-DC/OT-II CD4$^+$ T-cell co-culture was treated with a blocking anti-mouse MHC-II antibody (clone M5/114; 2 μg/mL; Additional file 1: Table S3). Surface CD40L expression was quantified within the 7-AAD$^-$CD3$^+$CD4$^+$ T-cell population by flow cytometry.

To assess CD4$^+$ T-cell help-dependent OT-I CD8$^+$ T-cell responses, OT-II CD4$^+$ T cells and OT-I CD8$^+$ T cells were co-cultured with LPS-stimulated DCs at a DC:CD4$^+$:CD8$^+$ cell ratio of 1:10:10 in the presence of full-length OVA (2 μg/mL) for 72 h. Experimental groups included OT-II CD4$^+$ and OT-I CD8$^+$ T cells cultured with OVA but without DCs; both T-cell subsets co-cultured with EV BVO-DCs, BM-DCs, or β-cat^{OE} BVO-DCs; β-cat^{OE} BVO-DCs co-cultured with OT-I CD8$^+$ T cells in the absence of OT-II CD4$^+$ T cells; and the complete β-cat^{OE} BVO-DC/OT-II CD4$^+$/OT-I CD8$^+$ T-cell tri-culture treated with a blocking anti-CD40L antibody (clone MR-1; 5 μg/mL; Additional file 1: Table S3). For proliferation analysis, OT-I CD8$^+$ T cells were labeled with CellTrace Violet before co-culture. Following the 72 h culture period, cells were stained with 7-AAD, CD4–Alexa Fluor 647, and CD8–PE. OT-I CD8$^+$ cells were identified as the 7-AAD$^-$CD4$^-$CD8$^+$ population, and proliferation was quantified by CellTrace Violet dilution within this population using the upstream gating strategy shown in Additional file 1: Figure S9A. For activation-marker analysis, corresponding parallel tri-cultures were established using OT-I CD8$^+$ T cells not labeled with CellTrace Violet. CD25 and PD-1 were assessed in separate staining tubes using 7-AAD, CD4–Pacific Blue, and CD8–PE together with either CD25–APC or PD-1–APC. The frequencies of CD25$^+$ and PD-1$^+$ cells were quantified within the 7-AAD$^-$CD4$^-$CD8$^+$ population using the upstream gating strategy shown in Additional file 1: Figure S9B.

Transcriptomic Profile Construction and Bioinformatic Analysis

Total RNA was extracted from primary BM-DCs, EV BVO-DCs, and β-cat^{OE} BVO-DCs using the RNAsimple Total RNA Kit according to the manufacturer's instructions (Additional file 1: Table S1). Four independent biological replicates were prepared for each group, yielding 12 samples in total. RNA quality assessment, strand-specific mRNA library preparation using the Illumina Stranded mRNA Prep, Ligation kit, and sequencing on an Illumina NovaSeq platform were performed by Shanghai Majorbio Bio-pharm Technology Co., Ltd. (Shanghai, China). Bioinformatic analyses were subsequently performed by the authors.

After quality filtering, clean reads were aligned to the mouse GRCm38/mm10 reference genome using Rsubread (version 2.26.0), and gene-level count matrices were generated using the featureCounts function implemented in Rsubread. Differential expression analysis was performed using DESeq2 (version 1.52.0) [22]. Genes with counts greater than 1 in at least four samples were retained. Differentially expressed genes were defined by a Benjamini–Hochberg-adjusted P value < 0.05 and $|\log_2$ fold change$| \geqslant 1$. Variance-stabilized expression values were used for principal component analysis and unsupervised hierarchical clustering of the 1,000 most highly variable genes. Row-wise Z-score heatmaps were generated using pheatmap (version 1.0.13). Gene Set Enrichment Analysis (GSEA) was performed using clusterProfiler (version 4.20.0), with genes ranked by the DESeq2 Wald statistic and gene sets obtained from Mouse MSigDB (version 2026.1.Mm). Gene Ontology Biological Process over-representation analysis was performed separately using the upregulated differentially expressed genes. Pairwise comparisons included EV BVO-DCs versus BM-DCs and β-cat^{OE} BVO-DCs versus EV BVO-DCs. All analyses were performed in R (version 4.6.0), with the software, databases, and reference genome listed in Additional file 1: Table S5.

CLP Model, Pulmonary BVO-DC Administration, and In Vivo Bioluminescence Imaging

All animal procedures were approved by the Institutional Animal Care and Use Committee of the Institute of Health and Medicine, Hefei Comprehensive National Science Center (approval no. IHM-AP-2025-093) and were performed in accordance with relevant institutional guidelines. Specific-pathogen-free male BALB/c mice (6–8 weeks old, 20–22 g) were obtained from Shanghai Model Organisms Center, Inc. (Additional file 1: Table S1) and randomly assigned to the Sham, CLP, CLP + EV BVO-DC, or CLP + β-cat^{OE} BVO-DC group. Separate cohorts were used for bioluminescence imaging, 48-h endpoint analyses, and 96-h survival analysis.

Polymicrobial sepsis was induced by cecal ligation and puncture (CLP) as previously described with modifications [23]. Mice were anesthetized by intraperitoneal administration of fluanisone (3.33 mg/kg) and diazepam (5 mg/kg; Additional file 1: Table S1). Anesthetic depth was confirmed by the absence of the pedal withdrawal reflex before skin incision and was assessed throughout surgery. A 1-cm

midline laparotomy was performed, and the cecum was exteriorized and ligated at the midpoint between the distal tip and the ileocecal valve using a 4-0 silk suture. The cecum was punctured twice with a 21-gauge needle, and a small amount of fecal material was extruded. The cecum was then returned to the abdominal cavity, and the incision was closed. Sham-operated mice underwent the same laparotomy and cecal manipulation without ligation or puncture. Following surgery, all mice received 1 mL of prewarmed sterile saline subcutaneously for fluid resuscitation and a single subcutaneous dose of buprenorphine hydrochloride (1 mg/kg) for postoperative analgesia (Additional file 1: Table S1). One hour after resuscitation, while still anesthetized, mice assigned to the treatment groups received EV BVO-DCs or β-cat^{OE} BVO-DCs intranasally at a dose of 1×10^7 cells in 50 μL of phosphate-buffered saline (PBS), with 25 μL administered into each nostril. Sham and CLP control mice received an equivalent volume of PBS. Clinical status was monitored hourly until the applicable humane or prespecified experimental endpoint. Humane endpoints were assessed using a previously described cageside scoring system in which "activity and response to stimulus" and "eye appearance" were each scored from 0 to 3; a combined score of ≥5 was defined as the humane endpoint [24]. Animals reaching the humane endpoint were euthanized immediately, whereas the remaining animals were euthanized at their prespecified experimental endpoints. Euthanasia was performed by intraperitoneal administration of an overdose of phenobarbital sodium (200 mg/kg; Additional file 1: Table S1), and death was confirmed by the absence of spontaneous respiration and heartbeat. For the survival cohorts, animals euthanized upon reaching the humane endpoint were recorded as deaths at the time of euthanasia.

For in vivo tracking, Luc-EV BVO-DCs or Luc-β-cat^{OE} BVO-DCs were administered using the same dose and procedure. Independent cohorts were imaged once at 4, 24, 48, or 72 h after administration (n = 4 mice per group per time point). D-luciferin potassium salt (150 mg/kg; Additional file 1: Table S1) was administered intraperitoneally, and images were acquired 10 min later using an IVIS Lumina LT Series III system (Additional file 1: Table S5) under consistent acquisition settings. Thoracic bioluminescence signals were analyzed using Fiji (ImageJ version 1.54p). A fixed-size thoracic region of interest was applied to each animal, and integrated density was measured using identical settings. Values were divided by 10^5 for graphical

presentation and expressed in arbitrary units. A separate cohort was monitored for survival for 96 h after CLP (n = 15 mice per group).

Assessment of Pulmonary Injury and Inflammation

Mice assigned to endpoint analyses were euthanized 48 h after surgery. Lung tissues were allocated for wet-to-dry (W/D) ratio determination, histopathological examination, immunofluorescence staining, and MPO activity measurement. For W/D analysis, freshly collected lung tissue was weighed and dried at 80 °C for 72 h before calculating the wet-to-dry weight ratio. For histology, lung tissues were fixed in 4% paraformaldehyde, paraffin-embedded, sectioned at 5 μm, and subjected to hematoxylin and eosin staining (Additional file 1: Table S1). Histopathological injury was evaluated by an investigator blinded to group allocation using a previously described 0–5 scoring system [25]. Pulmonary neutrophil-associated inflammation was assessed by measuring MPO activity in lung homogenates. BALF was collected by tracheal cannulation and three sequential washes with 0.8 mL of ice-cold PBS. The recovered BALF was centrifuged at 400 × *g* for 10 min at 4 °C. Supernatants were analyzed for total protein using a BCA assay and for IL-1β, IL-6, and TNF-α using ELISA kits (Additional file 1: Table S1). BALF cell pellets were retained for flow cytometric analysis.

Assessment of Pulmonary T-Cell Responses

Paraffin-embedded lung sections were subjected to dual immunofluorescence staining using rat anti-mouse CD4 and rabbit anti-mouse CD8α antibodies, followed by the corresponding Alexa Fluor 488-conjugated anti-rat and Alexa Fluor 594-conjugated anti-rabbit secondary antibodies. Nuclei were counterstained with 4′,6-diamidino-2-phenylindole (DAPI) (Additional file 1: Table S1). Images were acquired from three non-consecutive sections per animal using an ImageXpress Micro Confocal High-Content Imaging System (Molecular Devices) under identical settings (Additional file 1: Table S5). Five randomly selected, non-overlapping fields were analyzed per section. $CD4^+$ and $CD8^+$ cell densities were quantified using Fiji and expressed as cells/mm². Measurements from all analyzed fields were averaged to obtain one value per animal.

Bronchoalveolar lavage fluid (BALF) cell pellets were stained with 7-AAD, anti-mouse CD3-Pacific Blue, anti-mouse CD4-PE, and anti-mouse CD8α-Alexa Fluor 647

antibodies (Additional file 1: Tables S1 and S3). After debris and doublet exclusion, 7-AAD$^-$ live cells were identified, followed by quantification of CD3$^+$ T cells within the live-cell population and CD4$^+$ and CD8$^+$ subsets within the CD3$^+$ population. The CD4$^+$/CD8$^+$ ratio was calculated separately for each mouse from its corresponding CD4$^+$ and CD8$^+$ frequencies. Flow cytometric data were acquired using a Navios EX flow cytometer (Additional file 1: Table S5).

Statistical Analysis

Quantitative data are presented as mean ± standard deviation (SD). Exact sample sizes are provided in the corresponding figure legends; unless otherwise specified, n represents independent biological replicates or individual animals. Two-group comparisons were performed using unpaired two-tailed Student's t-tests for independent samples and paired two-tailed Student's t-tests for matched samples. Comparisons among three or more independent groups were performed using ordinary one-way ANOVA followed by Tukey's multiple-comparisons test. Data involving two independent factors were analyzed using ordinary two-way ANOVA followed by Šídák's multiple-comparisons test. For experiments in which all treatment conditions were evaluated within the same experimental batch, matched data were analyzed using repeated-measures ANOVA. MHC-II expression under different DC and LPS conditions was analyzed using two-way repeated-measures ANOVA followed by Tukey's multiple-comparisons test. The matched co-culture experiments were analyzed using one-way repeated-measures ANOVA with the Geisser–Greenhouse correction, followed by Tukey-adjusted multiple comparisons between the indicated groups. Kaplan–Meier survival curves were compared using the log-rank (Mantel–Cox) test, with Bonferroni adjustment for prespecified pairwise comparisons. For RNA-sequencing analyses, differential expression was assessed using the Wald test implemented in DESeq2, and P values were adjusted using the Benjamini–Hochberg method. Statistical analyses were performed using GraphPad Prism 10.6.0. A two-sided P value < 0.05 was considered statistically significant. Significance is indicated as follows: ns, not significant; *$P < 0.05$; **$P < 0.01$; ***$P < 0.001$; and ****$P < 0.0001$.

Results

β-Catenin Overexpression Promotes the Hematopoietic Differentiation Potential of 3D BVOs to Enhance Progenitor Yields

To evaluate how β-catenin overexpression modulates hematopoietic differentiation within the BVO induction system, we established a multi-stage protocol integrating genetic modification at the mESC stage, and subsequent BVO-based vascular and hematopoietic co-induction. As outlined in Figure 1A, EV and β-cat^{OE} mESCs underwent embryoid body formation and mesodermal induction (Days 0−2), hematoendothelial specification (Days 2−5), endothelial sprouting in a 3D collagen I/Matrigel matrix (Days 5−8), and vascular tubulogenesis with hematopoietic emergence (Days 8−11).

To track the morphological evolution and characterize the cellular architecture of developing BVOs, we performed serial phase-contrast imaging throughout differentiation, followed by cleared whole-mount confocal microscopy and multiparameter flow cytometry on Day 8. Serial phase-contrast imaging showed that undifferentiated mESC colonies formed compact EBs by Day 2 and enlarged spheroids by Day 5. Following embedding in collagen I/Matrigel, extensive cellular sprouts extended into the surrounding matrix by Day 8, accompanied by the appearance of phase-bright, rounded hematopoietic-like cells (Figure 1B, red arrow). Whole-mount confocal imaging demonstrated CD31$^+$ endothelial structures associated with PDGFR-β$^+$ perivascular cells and collagen IV deposition (Figure 1C).

At Day 8, vascular and hematopoietic cell subpopulation frequencies within the BVOs were evaluated via flow cytometry (Figures 1D and 1E), where all group means were calculated relative to the total 7-aminoactinomycin D-negative (7-AAD$^-$) live cell population following the upstream viable singlet-cell gating strategy shown in Additional file 1: Figure S1. For Flk-1$^+$VE-cadherin$^+$ hemogenic endothelial cells (HECs), PDGFR-β$^+$ pericytes, and CD31$^+$ endothelium, plot frequencies stood at 7.28%, 8.49%, and 11.25%, with corresponding group means of (7.32 ± 0.94)%, (8.21 ± 1.15)%, and (10.98 ± 1.84)%, respectively. Within the hematopoietic compartment, the initial CD117$^+$ gate registered 19.78% [group mean: (17.25 ± 2.12)%]. Sequential gating within the CD117$^+$ cells resolved the Lin$^-$ fraction at 97.73% (Figure 1D), within which the terminal Lin$^-$CD117$^+$CD43$^+$CD45$^+$ hematopoietic progenitor cell (HPC) subset

registered an internal parent-gate frequency of 6.63% (Figure 1D), corresponding to a group mean of (1.22 ± 0.24)% (Figure 1E). These findings indicate that Day 8 BVOs contained organized endothelial and perivascular components together with an emerging hematopoietic progenitor population.

We established stable β-catenin-overexpressing mESCs (β-cat^{OE} mESCs) via transduction of a lentiviral vector containing the full-length mouse Ctnnb1 coding sequence (Additional file 1: Figure S2A). RT-qPCR and Western blot analysis verified the robust upregulation of β-catenin in β-cat^{OE} mESCs compared to empty vector control mESCs (EV mESCs); specifically, Ctnnb1 mRNA expression registered 24.65 ± 5.90 vs. 0.99 ± 0.10 ($P < 0.001$; Figure 1F), while relative protein abundance (92 kDa) reached 2.71 ± 0.26 vs. 1.00 ± 0.11 ($P < 0.01$; Figure 1G). Meanwhile, RT-qPCR analysis confirmed that this genetic modification did not perturb the core endogenous pluripotency network, which remained conserved between EV mESCs and β-cat^{OE} mESCs for Nanog (1.03 ± 0.08 vs. 1.00 ± 0.08), Sox2 (0.96 ± 0.08 vs. 1.00 ± 0.08), and Oct4 (1.07 ± 0.07 vs. 1.00 ± 0.03) (Additional file 1: Figure S2B). High-resolution immunofluorescence tracking corroborated that both the EV mESCs and the ZsGreen-co-expressing β-cat^{OE} mESCs retained their tightly packed, undifferentiated colony architectures, with Nanog, Oct4, and Sox2 co-localized with nuclear staining (Additional file 1: Figure S2C).

To capture the peak window of hematopoietic progenitor commitment, we extended the BVO induction period to Day 11, generated EV and β-cat^{OE} BVOs from their respective mESCs, and determined how β-catenin overexpression modulates the vascular and hematopoietic lineages. Morphological characterization on Day 11 revealed that while the EV BVOs developed typical vascular channels with sparse cell shedding, the β-cat^{OE} BVOs exhibited dense sprouting architectures surrounded by clusters of emerging hematopoietic cells (Figure 1H, red arrows). At Day 11, vascular and hematopoietic cell subpopulation frequencies within EV BVOs and β-cat^{OE} BVOs were evaluated via flow cytometry and cumulative group analysis (Figures 1I–1K), where all group means were calculated relative to the 7-AAD^{-} live cell population. Notably, the structural vascular and perivascular lineages did not differ significantly between the two groups, registering representative plot values of 12.88% vs. 14.14% for Flk-1^{+}VE-cadherin^{+} HECs [group mean: (12.62 ± 1.37)% vs. (13.78 ± 2.43)%],

15.52% vs. 16.55% for PDGFR-β^+ pericytes [group mean: (13.84 ± 2.34)% vs. (16.02 ± 1.97)%], and 16.94% vs. 19.91% for $CD31^+$ vascular endothelial cells [group mean: (15.63 ± 1.78)% vs. (18.30 ± 2.89)%], respectively (Figures 1I–1K). In contrast, the hematopoietic compartment was markedly expanded under β-catenin overexpression; specifically, the Lin^-CD117^+ early hematopoietic progenitor pool increased from a calculated representative frequency of 22.48% [group mean: (21.12 ± 2.53)%] in EV BVOs to 54.26% in β-cat^{OE} BVOs [group mean: (52.83 ± 6.90)%] ($P < 0.0001$; Figures 1I–1K). Subsequent sequential hierarchical gating within this progenitor population resolved the terminal $Lin^-CD117^+CD43^+CD45^+$ HPC subset, which registered internal parent-gate frequencies of 18.93% in EV BVOs (Figure 1I) and 22.55% in β-cat^{OE} BVOs (Figure 1J), corresponding to a significantly higher normalized group mean of (11.96 ± 1.55)% in the β-cat^{OE} BVO group compared with (4.30 ± 0.53)% in the EV control ($P < 0.01$; Figures 1I–1K).

Concurrently, absolute cell counting demonstrated that β-cat^{OE} BVOs yielded an increased total cell count of (12.52 ± 1.43) × 10^7 cells per culture configuration, compared to the EV BVO control group which yielded (8.42 ± 1.57) × 10^7 cells ($P < 0.01$; Figure 1L). Collectively, these data support the successful derivation of β-cat^{OE} BVOs and demonstrate that β-catenin overexpression increased the frequency of phenotypically defined HPCs and the total cellular yield during BVO differentiation.

Efficient Derivation of β-cat^{OE} BVO-Derived DCs via Sustained β-Catenin Overexpression Across the mESC-BVO-HPC-DC Differentiation Process

To generate β-cat^{OE} BVO-derived DCs in vitro, we established a stepwise workflow using BVO-derived CHPC-enriched cells. As outlined in Figure 2A, 3D Col I/Matrigel BVOs were dissociated into single-cell suspensions, followed by positive immunomagnetic enrichment of $CD45^+$ hematopoietic cells and sequential early (Days 1–4) and late-stage (Days 4–8) DC differentiation, generating EV BVO-DCs and β-cat^{OE} BVO-DCs for subsequent flow cytometric and Western blot analyses.

We performed positive immunomagnetic enrichment of $CD45^+$ hematopoietic cells from dissociated BVO single-cell suspensions, followed by flow cytometry and Western blot analysis to characterize their phenotypic composition and β-catenin expression. The upstream gating strategy used to identify 7-AAD^- viable singlets after $CD45^+$ enrichment is shown in Additional file 1: Figure S3. The resulting cytometric

profiles showed that within the EV BVO group, $CD43^{+}CD45^{+}$ cells accounted for 99.20%, within which the Lin^{-} fraction was resolved at 93.85%, further yielding 27.31% $CD117^{+}$ cells; in parallel, the β-cat^{OE} BVO group exhibited a similar phenotypic profile, showing 97.79% $CD43^{+}CD45^{+}$ cells, within which the Lin^{-} fraction was 93.77%, further yielding 30.53% $CD117^{+}$ cells (Figure 2B). The CD45-enriched $Lin^{-}CD43^{+}CD45^{+}$ population contained both $CD117^{+}$ and $CD117^{-}$ fractions, indicating phenotypic heterogeneity following BVO dissociation and enrichment. This population was operationally designated as the CHPC-enriched population. Normalized to the total 7-AAD^{-} live-cell population, the phenotypically defined $Lin^{-}CD43^{+}CD45^{+}$ CHPC-enriched population, containing both $CD117^{+}$ and $CD117^{-}$ fractions, accounted for (90.87 ± 4.48)% in EV BVOs and (88.92 ± 5.10)% in β-cat^{OE} BVOs, with no significant difference between the two groups ($P = 0.5871$; Figure 2C). Western blot analysis and corresponding densitometric quantification confirmed a significant upregulation of β-catenin protein expression (92 kDa) in β-cat^{OE} BVO-CHPCs relative to EV BVO-CHPCs (1.69 ± 0.03 vs. 1.00 ± 0.02, $P < 0.0001$; Figures 2D and 2E). These results demonstrate that $CD45^{+}$ selection yielded CHPC-enriched populations in both groups without a significant difference in frequency, while β-catenin expression remained elevated in β-cat^{OE} BVO-CHPCs.

To differentiate EV and β-cat^{OE} BVO-derived CHPC-enriched cells into DCs, we applied a two-stage differentiation protocol and evaluated characteristic DC-associated surface markers. The common gating strategy used to identify 7-AAD^{-} viable singlets in the Day 4 and Day 8 DC differentiation cultures is shown in Additional file 1: Figure S4. On Day 4, flow cytometry of the culture suspensions showed that $CD11b^{+}CD11c^{+}$ cells accounted for 42.53% in the EV BVO-CHPC group and 50.52% in the β-cat^{OE} BVO-CHPC group (Figure 2F). Subsequently, cells from both groups underwent $CD11c^{+}$ magnetic enrichment and were cultured under late-stage DC differentiation conditions from Days 4 to 8. On Day 8, multiparameter flow cytometry characterized the resulting DC-associated phenotypic profiles. For cells derived from EV BVO-CHPCs, $CD11b^{+}CD11c^{+}$ cells reached 94.07%, within which the frequencies of MHC-II^{+}, $CD86^{+}$, and $CD80^{+}$ cells were 13.42%, 10.02%, and 11.81%, respectively. In parallel, cells derived from β-cat^{OE} BVO-CHPCs reached 98.08% $CD11b^{+}CD11c^{+}$ cells, with corresponding frequencies of 23.88%, 11.87%, and 12.01%, respectively (Figure

2F). Separate quantitative group analysis normalized to the total 7-AAD$^-$ live-cell population showed that the group means for CD11b$^+$CD11c$^+$CD86$^+$ cells [(12.39 ± 2.03)% vs. (14.70 ± 2.22)%] and CD11b$^+$CD11c$^+$CD80$^+$ cells [(14.05 ± 2.20)% vs. (14.23 ± 2.25)%] did not differ significantly between the EV and β-cat^{OE} groups (Figure 2G). However, the group mean proportion of CD11b$^+$CD11c$^+$MHC-II$^+$ cells was significantly higher in the β-cat^{OE} BVO-DC group than in the EV BVO-DC group [(19.47 ± 3.19)% vs. (15.39 ± 2.26)%, $P < 0.01$; Figure 2G]. Collectively, these data support the differentiation of EV and β-cat^{OE} BVO-derived CHPC-enriched cells into phenotypically defined BVO-derived DCs expressing characteristic DC-associated surface markers.

To determine whether engineered β-catenin overexpression was maintained through late-stage DC differentiation, we performed Western blot analysis of Day 8 BVO-derived DCs. This analysis and corresponding densitometric quantification revealed that β-cat^{OE} BVO-DCs retained higher β-catenin protein abundance than EV BVO-DCs (2.89 ± 0.73 vs. 1.00 ± 0.19, $P < 0.05$; Figures 2H and 2I). Taken together, these findings demonstrate that mESC-stage β-catenin overexpression was maintained at the assessed CHPC and Day 8 BVO-DC stages, supporting the successful in vitro generation of β-cat^{OE} BVO-derived DCs.

β-cat^{OE} BVO-DCs Promote CD8$^+$ T Cell Proliferation and Activation via the MHC-II/CD4$^+$ T/CD40L Axis

We established sequential DC/T-cell co-culture and tri-culture systems to evaluate the antigen-presenting function of β-cat^{OE} BVO-DCs and their capacity to promote downstream T-cell responses. As outlined in Figure 3A, EV BVO-DCs, primary BM-DCs, and β-cat^{OE} BVO-DCs were first stimulated with LPS for morphological and MHC-II phenotypic assessment. For the functional assays, DCs were initially co-cultured with OT-II CD4$^+$ T cells in a DC/CD4$^+$ T-cell co-culture system. OT-II CD4$^+$ T cells and OT-I CD8$^+$ T cells were subsequently combined with DCs in a DC/CD4$^+$/CD8$^+$ T-cell tri-culture system.

To assess the phenotypic maturation and morphological shifts triggered by inflammatory stimuli, we subjected the DCs to LPS activation followed by phase-contrast microscopy and flow cytometric analysis of MHC-II. Before use as a positive control, primary BM-DCs generated from mouse bone marrow were phenotypically

validated by flow cytometry (Additional file 1: Figure S5). Phase-contrast imaging showed that, under unstimulated conditions (−LPS), all three DC populations predominantly exhibited rounded or semi-suspended morphologies with limited dendritic-like projections. Under +LPS conditions, increased cellular clustering, adherence, and spreading were observed across the three groups. β-cat^{OE} BVO-DCs appeared to exhibit more pronounced spreading and dendritic-like projections than EV BVO-DCs and BM-DCs (Figure 3B). MHC-II expression was subsequently quantified within the 7-AAD^{-}CD11b^{+}CD11c^{+} population using the upstream gating strategy shown in Additional file 1: Figure S6. Under −LPS conditions, representative MHC-II^{+} frequencies were 10.29%, 14.41%, and 18.36% for EV BVO-DCs, BM-DCs, and β-cat^{OE} BVO-DCs, respectively, with corresponding group means of 9.85 ± 1.35%, 15.21 ± 0.69%, and 17.73 ± 3.25%. Both BM-DCs and β-cat^{OE} BVO-DCs showed higher MHC-II^{+} frequencies than EV BVO-DCs (Tukey-adjusted P = 0.0123 and 0.0081, respectively), whereas BM-DCs and β-cat^{OE} BVO-DCs did not differ significantly (adjusted P = 0.4075). Under +LPS conditions, the corresponding group means were 18.63 ± 2.88%, 26.74 ± 4.23%, and 47.73 ± 7.77%. BM-DCs showed a higher frequency than EV BVO-DCs (adjusted P = 0.0044), whereas β-cat^{OE} BVO-DCs showed higher frequencies than both EV BVO-DCs (adjusted P = 0.0027) and BM-DCs (adjusted P = 0.0039; Figures 3C and 3D). These results indicate that β-catenin overexpression is associated with an enhanced MHC-II^{+} DC phenotype, particularly under LPS-stimulated conditions.

To assess CD4^{+} T-cell activation in OVA-containing DC/CD4^{+} T-cell co-cultures and its sensitivity to MHC-II blockade, CD40L expression was quantified within the 7-AAD^{-}CD3^{+}CD4^{+} population using the upstream gating strategy shown in Additional file 1: Figure S8. CD4^{+} T cells cultured without DCs showed a representative CD40L^{+} frequency of 0.92% [group mean: 0.95 ± 0.14%]. The frequency increased to 14.51% in the EV BVO-DC group [12.28 ± 1.76%] and 25.93% in the BM-DC group [22.24 ± 2.85%], with a significant difference between the two groups (Tukey-adjusted P = 0.0169). The β-cat^{OE} BVO-DC group showed the highest CD40L^{+} frequency of 36.12% [35.37 ± 3.45%], which was significantly higher than those in the EV BVO-DC (adjusted P = 0.0075) and BM-DC (adjusted P = 0.0101) groups. MHC-II blockade reduced the CD40L^{+} frequency to 14.25% [12.25 ± 1.59%], which was significantly

lower than that in the unblocked β-cat^{OE} BVO-DC group (adjusted P = 0.0070; Figure 3E). These findings indicate that β-cat^{OE} BVO-DCs enhance CD4$^+$ T-cell activation in OVA-containing co-cultures and that this response is sensitive to MHC-II blockade.

We next assessed OT-I CD8$^+$ T-cell proliferation in the OVA-containing DC/CD4$^+$/CD8$^+$ T-cell tri-culture system. CellTrace Violet-labeled OT-I CD8$^+$ cells were identified within the 7-AAD$^-$CD4$^-$CD8$^+$ population using the upstream gating strategy shown in Additional file 1: Figure S9A, and proliferation was quantified by CellTrace Violet dilution within this population. The T-cell-only group showed a representative proliferating CD8$^+$ T-cell frequency of 27.29% [group mean: 26.87 ± 3.57%]. The corresponding frequencies increased to 32.18% in the EV BVO-DC group [32.00 ± 5.88%] and 57.46% in the BM-DC group [54.55 ± 9.37%], with a significant difference between the two DC groups (Tukey-adjusted P = 0.0063). The β-cat^{OE} BVO-DC group showed the highest proliferation frequency of 80.93% [77.01 ± 7.46%], which was significantly higher than those in the EV BVO-DC (adjusted P = 0.0003) and BM-DC (adjusted P = 0.0016) groups. Omission of CD4$^+$ T cells or CD40L blockade reduced the proliferation frequency to 28.25% [27.82 ± 5.37%] and 32.91% [31.46 ± 6.41%], respectively (adjusted P = 0.0002 and 0.0010 vs. the complete β-cat^{OE} BVO-DC tri-culture; Figure 3F). These findings support CD4$^+$ T-cell- and CD40L-dependent enhancement of CD8$^+$ T-cell proliferation by β-cat^{OE} BVO-DCs.

Within the DC/CD4$^+$/CD8$^+$ T-cell tri-culture system, we further evaluated OT-I CD8$^+$ T-cell activation-associated phenotypes by measuring CD25 and PD-1 expression in separate staining tubes. Both markers were quantified within the 7-AAD$^-$CD4$^-$CD8$^+$ population using the upstream gating strategy shown in Additional file 1: Figure S9B. The T-cell-only group showed a representative CD25$^+$ frequency of 1.35% [group mean: 1.30 ± 0.13%]. This frequency increased to 19.22% in the EV BVO-DC group [18.83 ± 0.96%] and 36.37% in the BM-DC group [33.54 ± 4.32%], with a significant difference between the two DC groups (Tukey-adjusted P = 0.0164). The β-cat^{OE} BVO-DC group showed the highest CD25$^+$ frequency of 54.56% [51.84 ± 4.61%], which was significantly higher than those in the EV BVO-DC (adjusted P = 0.0020) and BM-DC (adjusted P < 0.0001) groups. Omission of CD4$^+$ T cells or CD40L blockade reduced the CD25$^+$ frequency to 11.28% [10.55 ± 1.95%] and 17.59% [16.48 ± 3.13%], respectively (adjusted P = 0.0004 and < 0.0001, respectively; Figure 3G).

In the separately stained PD-1 panel, the representative PD-1^{+} frequency was 3.70% in the T-cell-only group [group mean: 3.37 ± 0.49%], 11.27% in the EV BVO-DC group [11.70 ± 2.39%], and 35.20% in the BM-DC group [34.31 ± 6.56%], with a significant difference between the EV BVO-DC and BM-DC groups (Tukey-adjusted P = 0.0409). The β-cat^{OE} BVO-DC group showed a representative PD-1^{+} frequency of 54.25% [54.30 ± 5.71%], which was significantly higher than those in the EV BVO-DC (adjusted P = 0.0050) and BM-DC (adjusted P = 0.0001) groups. Omission of CD4^{+} T cells or CD40L blockade reduced the PD-1^{+} frequency to 8.80% [8.47 ± 1.60%] and 14.37% [13.75 ± 2.81%], respectively (adjusted P = 0.0012 and 0.0007 vs. the complete β-cat^{OE} BVO-DC tri-culture; Figure 3H). In this short-term assay, PD-1 upregulation was interpreted as activation-associated checkpoint induction rather than evidence of T-cell exhaustion.

Collectively, these findings indicate that β-cat^{OE} BVO-DCs enhance CD4^{+} T-cell activation and promote CD8^{+} T-cell proliferation and activation-associated phenotypes in OVA-containing co-cultures. The effects of MHC-II blockade, CD4^{+} T-cell omission, and CD40L blockade support the involvement of MHC-II-sensitive CD4^{+} T-cell activation and CD40L-dependent T-cell help.

β-Catenin Overexpression Reprograms the BVO-DC Transcriptome to Restore Wnt Signaling and MHC-Mediated Antigen Presentation

To characterize the global transcriptomic shifts driven by β-catenin enrichment, high-throughput RNA sequencing (RNA-seq) was performed on EV BVO-DCs, BM-DCs, and β-cat^{OE} BVO-DCs. Unsupervised hierarchical clustering of the top 1000 highly variable genes (HVGs) resolved distinct expression profiles across groups. Compared with primary BM-DCs, a prominent gene cluster was extensively downregulated in EV BVO-DCs but robustly upregulated in β-cat^{OE} BVO-DCs, exceeding even BM-DC reference levels (Figure 4A). Pairwise volcano plot profiling identified a widespread downregulation of core immunological and identity loci in EV BVO-DCs relative to primary BM-DCs, heavily suppressing Ctnnb1, Zbtb46, Relb, Cd80, H2-Aa, and H2-Ab1 (Figure 4B). Consistent with these findings, Gene Set Enrichment Analysis (GSEA) revealed negative enrichment of gene sets associated with Wnt signaling, dendritic cell differentiation, and MHC class I and II antigen presentation in EV BVO-DCs relative to BM-DCs (Figure 4C).

We performed Principal Component Analysis (PCA), pairwise volcano plot profiling, and Gene Ontology (GO) biological process enrichment to ascertain the overall transcriptomic variance and identify the specific molecular pathways activated by β-catenin overexpression. PCA—with PC1 and PC2 accounting for 49.47% and 21.04% of the total variance, respectively—revealed that while EV BVO-DCs exhibited a distinct transcriptional deviation relative to primary BM-DCs, the engineered β-cat^{OE} BVO-DCs shifted toward the BM-DC transcriptional profile but remained transcriptionally distinguishable (Figure 4D). Pairwise volcano plot profiling of β-cat^{OE} BVO-DCs versus EV BVO-DCs resolved a broad transcriptomic shift driven by β-catenin reinforcement, highlighting the significant upregulation of core downstream targets (Ctnnb1, Axin2, Tcf7) alongside key dendritic cell identity and maturation determinants (Zbtb46, Relb, Cd80, Cd74, H2-Aa, H2-Ab1, and H2-K1; Figure 4E). This targeted transcriptional reactivation was systematically substantiated by GO biological process enrichment analysis, which revealed a highly selective overrepresentation of upregulated transcripts within major antigen-presentation cascades, including peptide antigen assembly with MHC class II protein complex, MHC class II protein complex assembly, and antigen processing and presentation of exogenous peptide antigen via MHC class II (Figure 4F).

To granularly resolve the expression patterns across specific functional modules, we executed targeted heatmap profiling of the Wnt signaling and MHC-mediated antigen presentation pathways. Within the Wnt Signaling Pathway module, β-cat^{OE} BVO-DCs drove a robust transcriptional reactivation of core effectors (Tcf7, Ccnd1, Dvl3, Ctnnb1, Axin2, Tcf7l2) that inverted the baseline deficiency observed in empty-vector controls. Strikingly, this molecular override concurrently triggered the broad up-regulation of the Dendritic Cell Differentiation program (Stat3, Relb, Cd74, Zbtb46, Nfkb1, Cd80) and the increased expression of MHC Class I and II Molecules (H2-K1, H2-D1, H2-DMa, H2-Eb2, H2-Eb1, H2-Ab1, H2-Aa, H2-DMb1), with expression levels in the engineered group systematically matching or exceeding the BM-DC reference levels (Figure 4G). Altogether, these transcriptomic analyses indicate that mESC-stage β-catenin overexpression shifts BVO-DCs toward a BM-DC-like transcriptional state relative to EV BVO-DCs, accompanied by enhanced expression of gene programs associated with canonical Wnt signaling, dendritic cell differentiation,

and MHC class I and II antigen presentation.

β-cat^{OE} BVO-DCs Alleviate Sepsis-Induced Acute Lung Injury

To characterize the time-dependent pulmonary bioluminescence signals of EV and β-cat^{OE} BVO-DCs, luciferase-expressing EV BVO-DCs (Luc-EV BVO-DCs) and β-cat^{OE} BVO-DCs (Luc-β-cat^{OE} BVO-DCs) were generated through the BVO–CHPC–DC differentiation pipeline, administered intranasally, and imaged in independent cohorts of mice at 4, 24, 48, or 72 h after administration. At 4 h, readily detectable bioluminescence signals were predominantly localized to the pulmonary regions in both groups, with the integrated density reaching $(6.29 \pm 0.31) \times 10^5$ a.u. for the Luc-EV BVO-DC group and $(6.29 \pm 0.14) \times 10^5$ a.u. for the Luc-β-cat^{OE} BVO-DC group, demonstrating no statistically significant difference and indicating comparable early pulmonary signal levels (Figures 5A and 5B). Notably, at the intermediate time points of 24 and 48 h, the Luc-β-cat^{OE} BVO-DC group maintained a significantly higher bioluminescence intensity than the Luc-EV BVO-DC group, with integrated density values of $(4.14 \pm 0.30) \times 10^5$ a.u. versus $(2.42 \pm 0.31) \times 10^5$ a.u. at 24 h ($P < 0.0001$) and $(2.69 \pm 0.10) \times 10^5$ a.u. versus $(0.87 \pm 0.10) \times 10^5$ a.u. at 48 h ($P < 0.0001$), respectively (Figures 5A and 5B). By the 72 h time point, the integrated density values declined to $(0.34 \pm 0.13) \times 10^5$ a.u. for the Luc-EV BVO-DC group and $(0.57 \pm 0.25) \times 10^5$ a.u. for the Luc-β-cat^{OE} BVO-DC group, with no statistically significant difference between the two groups (Figures 5A and 5B). These findings indicate that β-catenin overexpression is associated with greater persistence of BVO-DC-derived pulmonary bioluminescence signals at 24 and 48 h after administration.

To evaluate the therapeutic efficacy of β-cat^{OE} BVO-DCs in polymicrobial sepsis, mice underwent CLP surgery followed by BVO-DC treatment, and survival was monitored for 96 h. Kaplan–Meier survival analysis showed estimated 96 h survival probabilities of 100%, 13.3%, 20.0%, and 53.3% in the Sham, CLP, CLP + EV BVO-DCs, and CLP + β-cat^{OE} BVO-DCs groups, respectively. Survival did not differ significantly between the CLP and CLP + EV BVO-DCs groups (Bonferroni-adjusted log-rank $P = 1.000$). In contrast, survival was significantly improved in the CLP + β-cat^{OE} BVO-DCs group compared with both the CLP group (adjusted $P = 0.0078$) and the CLP + EV BVO-DCs group (adjusted $P = 0.0385$; Figure 5C). These findings indicate that β-cat^{OE} BVO-DC treatment improves survival in CLP-induced septic mice.

To investigate the histopathological changes and assess the extent of structural tissue protection afforded by β-cat^{OE} BVO-DCs, lung tissues were collected 48 h after CLP or sham surgery for hematoxylin and eosin (H&E) staining and pathological scoring. The Sham group maintained an intact alveolar architecture with a baseline injury score of 0.20 ± 0.04. Conversely, the untreated CLP group exhibited severe alveolar septal thickening, dense inflammatory infiltration, and alveolar collapse, with the score escalating to 3.55 ± 0.25 ($P < 0.0001$ vs. Sham). The injury score in the CLP + EV BVO-DC group did not differ significantly from that in the CLP group (3.26 ± 0.36, $P > 0.05$ vs. CLP). In contrast, the CLP + β-cat^{OE} BVO-DC treatment group showed better-preserved alveolar architecture, reduced inflammatory-cell infiltration, and a lower pathological score to 1.49 ± 0.19 ($P < 0.0001$ vs. both CLP and CLP + EV BVO-DC; Figures 5D and 5E). These findings demonstrate that β-cat^{OE} BVO-DCs possess protective effects in preserving pulmonary structural integrity and mitigating sepsis-induced acute lung injury.

To assess pulmonary edema, alveolar–capillary barrier leakage, and neutrophil-associated inflammation, we measured the lung wet-to-dry (W/D) weight ratio, BALF total protein concentration, and lung myeloperoxidase (MPO) activity at 48 h after surgery. The Sham group established stable baseline parameters across all three indices, registering a W/D ratio of 3.06 ± 0.42, a BALF protein concentration of (0.20 ± 0.03) mg/mL, and an MPO activity of (1.64 ± 0.15) U/g. Sepsis induction in the CLP group elevated these metrics to (5.67 ± 0.53), (2.54 ± 0.12) mg/mL, and (13.21 ± 0.66) U/g, respectively ($P < 0.0001$ vs. Sham). These pathological elevations were only partially mitigated in the CLP + EV BVO-DC control group, which retained a high W/D ratio of 5.01 ± 0.61 ($P > 0.05$ vs. CLP), a BALF total protein concentration of (2.33 ± 0.09) mg/mL ($P < 0.01$ vs. CLP), and an MPO activity of (12.00 ± 0.82) U/g ($P < 0.05$ vs. CLP). In contrast, the CLP + β-cat^{OE} BVO-DC treatment group significantly reduced all three injury-related parameters with the W/D ratio to 3.69 ± 0.52 ($P < 0.0001$ vs. CLP; $P < 0.01$ vs. CLP + EV BVO-DC), the BALF total protein concentration to (1.14 ± 0.08) mg/mL ($P < 0.0001$ vs. CLP and CLP + EV BVO-DC), and the localized tissue MPO activity to (6.36 ± 0.83) U/g ($P < 0.0001$ vs. CLP and CLP + EV BVO-DC; Figures 5F–5H).

To map the localized pulmonary inflammatory response within the alveolar space,

we performed enzyme-linked immunosorbent assay (ELISA) to determine the concentrations of key pro-inflammatory cytokines in the BALF. The Sham group showed baseline IL-1β, IL-6, and TNF-α concentrations of (39.19 ± 4.06), (7.00 ± 4.34), and (52.50 ± 9.35) pg/mL, respectively. The corresponding concentrations in the untreated CLP group increased to (935.20 ± 42.60), (199.50 ± 15.86), and (1230.00 ± 85.79) pg/mL, respectively ($P < 0.0001$ vs. Sham). This localized inflammatory response was only partially mitigated in the CLP + EV BVO-DC control group, which retained an elevated IL-1β level [(880.60 ± 50.36) pg/mL, $P > 0.05$ vs. CLP], while showing modest but significant reductions in IL-6 [(173.00 ± 12.31) pg/mL, $P < 0.05$ vs. CLP] and TNF-α [(1120.00 ± 81.73) pg/mL, $P < 0.05$ vs. CLP]. In contrast, the CLP + β-cat^{OE} BVO-DC group significantly reduced BALF IL-1β to (377.90 ± 31.38) pg/mL, IL-6 to (57.50 ± 15.82) pg/mL, and TNF-α to (465.00 ± 64.73) pg/mL [$P < 0.0001$ vs. both CLP and CLP + EV BVO-DC; Figures 5I–5K].

Collectively, β-cat^{OE} BVO-DC treatment was associated with higher pulmonary bioluminescence signals at 24 and 48 h, improved 96 h survival, and reduced CLP-induced pulmonary injury and BALF inflammatory cytokine concentrations.

β-cat^{OE} BVO-DCs Restore Pulmonary CD8$^+$ T-Cell Abundance and CD4$^+$/CD8$^+$ Balance in Sepsis-Induced Acute Lung Injury

To visualize the spatial distribution and quantify the tissue densities of CD4$^+$ and CD8$^+$ T cells in lung tissue, we performed multiplex immunofluorescence confocal imaging followed by quantitative image analysis at 48 h after CLP or sham surgery. This spatial analysis revealed that the Sham group showed a scattered distribution of CD4$^+$ T cells [group mean: (442.83 ± 31.37) cells/mm²] and CD8$^+$ T cells [group mean: (330.31 ± 25.12) cells/mm²] within the lung parenchyma. In contrast, CLP induction markedly reduced the tissue densities of both subsets, reducing the densities to (109.38 ± 18.75) cells/mm² for CD4$^+$ T cells and (69.03 ± 11.13) cells/mm² for CD8$^+$ T cells ($P < 0.0001$ vs. Sham for both comparisons). The CLP + EV BVO-DC control group partially increased the CD4$^+$ T-cell density to (200.46 ± 19.45) cells/mm² ($P < 0.01$ vs. CLP), whereas the CD8$^+$ T-cell density remained at (77.96 ± 15.65) cells/mm² and did not differ significantly from that in the CLP group ($P > 0.05$). The CLP + β-cat^{OE} BVO-DC treatment group increased the tissue densities of both populations, reaching (407.02 ± 30.48) cells/mm² for CD4$^+$ T cells and (290.67 ± 14.89) cells/mm² for CD8$^+$ T cells;

both densities were significantly higher than the corresponding densities in the CLP and CLP + EV BVO-DC groups ($P < 0.0001$ for each comparison) (Figures 6A–6C).

We further examined the frequencies of $CD4^+$ and $CD8^+$ T cells within the bronchoalveolar lavage fluid (BALF) by performing multiparameter flow cytometric profiling. Sequential gating first identified 7-AAD^- live cells, followed by $CD3^+$ T cells; the $CD4^+$ and $CD8^+$ T-cell subsets were then resolved within the $CD3^+$ gate, with representative flow plots and quantitative group analyses shown in Figures 6D–6I. Specifically, the frequency of 7-AAD^- live cells among singlets decreased from a representative 92.50% in the Sham group [group mean: (93.81 ± 2.09)%] to 57.14% in the CLP group [group mean: (57.73 ± 4.05)%] ($P < 0.0001$). The corresponding frequency in the CLP + EV BVO-DC group was 71.34% [group mean: (64.53 ± 5.10)%] and did not differ significantly from that in the CLP group ($P > 0.05$), whereas the CLP + β-cat^{OE} BVO-DC treatment group increased this frequency to 82.39% [group mean: (82.05 ± 2.13)%] ($P < 0.0001$ vs. CLP; $P < 0.001$ vs. CLP + EV BVO-DC; Figure 6E). Similarly, the $CD3^+$ T-cell fraction within the 7-AAD^- live-cell gate decreased from a representative 4.90% in the Sham group [group mean: (4.71 ± 0.51)%] to 3.12% in the CLP group [group mean: (3.20 ± 0.19)%] ($P < 0.001$). The CLP + EV BVO-DC group showed a comparable frequency of 3.43% [group mean: (3.33 ± 0.41)%] ($P > 0.05$ vs. CLP), whereas the CLP + β-cat^{OE} BVO-DC treatment group increased this fraction to 4.63% [group mean: (4.35 ± 0.38)%] ($P < 0.01$ vs. CLP; $P < 0.05$ vs. CLP + EV BVO-DC; Figure 6F).

We next compared the frequencies of $CD4^+$ and $CD8^+$ T cells within the $CD3^+$ population and calculated the corresponding $CD4^+/CD8^+$ ratios to evaluate T-cell distribution and balance within the BALF. CLP induction reduced the $CD4^+$ T-cell frequency from a representative 58.58% in the Sham group [group mean: (56.24 ± 7.23)%] to 44.60% in the CLP group [group mean: (39.65 ± 3.86)%] ($P < 0.01$). The CLP + EV BVO-DC group showed an increased $CD4^+$ T-cell frequency of 50.34% [group mean: (49.98 ± 3.32)%] ($P < 0.05$ vs. CLP), whereas the CLP + β-cat^{OE} BVO-DC treatment group showed a frequency of 52.97% [group mean: (51.28 ± 3.63)%] ($P < 0.05$ vs. CLP; $P > 0.05$ vs. CLP + EV BVO-DC; Figure 6G). In parallel, the $CD8^+$ T-cell frequency decreased from a representative 25.80% in the Sham group [group mean: (25.04 ± 3.28)%] to 9.65% in the CLP group [group mean: (10.04 ± 1.46)%] ($P <$

0.0001). The $CD8^+$ T-cell frequency in the CLP + EV BVO-DC group was 13.78% [group mean: (12.15 ± 3.01)%] and did not differ significantly from that in the CLP group ($P > 0.05$), whereas the CLP + β-cat^{OE} BVO-DC treatment group increased the $CD8^+$ T-cell frequency to 25.30% [group mean: (24.63 ± 3.11)%] ($P < 0.0001$ vs. CLP; $P < 0.001$ vs. CLP + EV BVO-DC; Figure 6H). Accordingly, the representative $CD4^+/CD8^+$ ratio increased from 2.27 in the Sham group [group mean: (2.25 ± 0.17)] to 4.62 in the CLP group [group mean: (4.01 ± 0.69)] ($P < 0.05$). This ratio remained elevated in the CLP + EV BVO-DC group at 3.65 [group mean: (4.31 ± 1.10)] ($P > 0.05$ vs. CLP) but was reduced toward the Sham level in the CLP + β-cat^{OE} BVO-DC group to 2.09 [group mean: (2.12 ± 0.40)] ($P < 0.01$ vs. CLP; $P < 0.01$ vs. CLP + EV BVO-DC; Figure 6I). Collectively, β-cat^{OE} BVO-DC treatment improved pulmonary T-cell abundance and rebalanced the BALF T-cell compartment by increasing the $CD8^+$ T-cell frequency and reducing the $CD4^+/CD8^+$ ratio toward Sham levels in CLP-induced acute lung injury.

An integrated schematic summarizing the β-cat^{OE} BVO-DC generation strategy, MHC-II-sensitive $CD4^+$ T-cell activation, CD40L-dependent $CD8^+$ T-cell proliferation and activation-associated phenotypes, and the therapeutic effects observed in CLP-induced acute lung injury is presented in Figure 7.

Discussion

In this study, we established a 3D vascular-hematopoietic co-development organoid platform (BVO platform) combined with β-catenin overexpression at the embryonic stem cell (mESC) stage, thereby achieving a more efficient in vitro expansion of hematopoietic progenitor cells (HPCs). Current strategies for constructing 3D vascular organoids, however, are predominantly tailored toward investigating basic vascular morphogenesis or modeling cardiovascular pathologies [26, 27], with expansion conditions optimized mainly to sustain endothelial and perivascular lineages [28, 29]. The emergence of hematopoietic stem and progenitor cells (HSPCs) relies on the endothelial-to-hematopoietic transition (EHT) [30], while in vitro HSPC generation requires defined hematopoietic cytokine cocktails to promote EHT and expansion [31, 32]. Nonetheless, conventional 3D vascular organoid platforms lack these essential stimuli, thereby limiting HSPC emergence and expansion. To bridge these deficits, we

leveraged EHT principles to conceptualize a 3D "vascular-hematopoietic co-development" strategy. By introducing a specialized hematopoietic cytokine cocktail into BVOs during critical developmental windows, we established a modified BVO platform that concurrently sustains 3D microvascular networks and hematopoietic differentiation.

During the hematopoietic specification window, Wnt signaling provides essential instructive cues for definitive hematopoietic differentiation of mESCs [33], with β-catenin acting as the central downstream effector that translocates into the nucleus to execute the corresponding transcriptional programs [34]. On the other hand, during in vitro mESC culture, stabilization of the Wnt/β-catenin cascade is indispensable for maintaining their undifferentiated self-renewal state [35]. Capitalizing on this dual role, we validated that its overexpression at the mESC stage successfully preserves undifferentiated stemness during in vitro culture, while significantly enhancing the generation efficiency of CHPCs during subsequent BVO induction, thereby highlighting the distinct methodological advantages of pluripotent-stage genetic engineering.

Wnt/β-catenin signaling in dendritic cells serves as an important regulator of immune function by controlling inflammatory responses, tolerance programs, and T-cell priming capacity [36]. Its immunological effects, however, appear to be highly context- and stage-dependent. In differentiated or tumor-associated DCs, β-catenin activation has been shown to induce IL-10- and Tim-3-associated tolerogenic programs that limit $CD8^+$ T-cell cross-priming and antitumor immunity [37, 38]. Meanwhile, the clinical translation of DC-based therapies remains constrained by the limited expansion capacity, short-term viability, and challenges associated with the genetic manipulation of primary DCs in vitro [39, 40]. Rather than directly manipulating β-catenin signaling in terminally differentiated DCs, we introduced β-catenin overexpression at the mESC stage, allowing its effects to be propagated through hematopoietic specification and subsequent DC differentiation. This strategy generated $\beta\text{-cat}^{OE}$ BVO-DCs that enhanced $CD8^+$ T-cell responses through MHC-II-dependent $CD4^+$ T-cell activation and CD40L-mediated DC licensing.

Accumulating evidence indicates that DC functional identity is progressively programmed during development rather than fixed at terminal maturation. Early

developmental cues can durably shape DC phenotypes and functional states [41], while PU.1-dependent chromatin remodeling and sequential activation of *Irf8* enhancers establish lineage-specific transcriptional programs [42]. In parallel, subset-specific metabolic programs regulate DC differentiation, survival, antigen presentation, and T-cell priming [43]. Against this background, our transcriptomic profiling indicated that mESC-stage β-catenin overexpression developmentally programmed BVO-derived DCs by restoring Wnt/β-catenin transcriptional activity and enhancing DC differentiation and antigen-presentation programs. These persistent changes suggest that mESC-stage β-catenin overexpression may establish a durable developmental state through chromatin remodeling, lineage-defining transcriptional networks, or metabolic adaptation. As this inference is based on terminal-stage transcriptomics, longitudinal multi-omic studies across the mESC-to-CHPC-to-DC trajectory are required for validation.

$CD8^+$ T-cell exhaustion, characterized by sustained expression of inhibitory receptors, impaired effector function, and reduced proliferative capacity, represents a critical mechanism underlying immune dysfunction during chronic infections and severe inflammatory disorders [44]. In sepsis, persistent antigen exposure and inflammatory stress drive $CD8^+$ T-cell exhaustion [45], contributing to impaired pathogen clearance, increased susceptibility to secondary infections, and poor clinical outcomes [46, 47]. Restoring $CD8^+$ T-cell function has therefore emerged as a potential strategy to reverse sepsis-associated immunosuppression and improve host immune competence. Capitalizing on this concept, our study demonstrates that $\beta\text{-cat}^{OE}$ BVO-DCs exhibited prolonged retention within septic lungs and conferred protection against CLP-induced sepsis by preserving alveolar integrity, restoring pulmonary barrier function, attenuating inflammatory responses, and reestablishing $CD4^+$ and $CD8^+$ T-cell homeostasis.

Despite the therapeutic potential of our platform, several limitations remain to be addressed for future clinical translation. First, our study was performed in a murine system using mESC-derived BVO-DCs and a CLP-induced sepsis model; therefore, validation in human pluripotent stem cell–derived systems and humanized models will be necessary to account for interspecies differences in immune regulation and Wnt signaling responses. Second, although intranasal delivery enabled efficient pulmonary

targeting and protection against ALI, further studies are required to evaluate the systemic distribution and therapeutic efficacy of β-cat^{OE} BVO-DCs in the context of sepsis-associated multi-organ dysfunction. Finally, although RNA-seq revealed that β-catenin overexpression enhances dendritic cell differentiation and MHC class I/II antigen presentation programs in β-cat^{OE} BVO-DCs, the precise molecular mechanisms linking these transcriptional changes to DC–T cell communication remain to be further defined.

Conclusions

In conclusion, our engineered 3D BVO system with mESC-stage β-catenin modification provides a developmental strategy to address the limited cellular availability and functional vulnerability of conventional DC preparations. In vitro blockade experiments support the involvement of the MHC-II/CD4^{+} T-cell/CD40L axis in the enhanced T-cell responses induced by β-cat^{OE} BVO-DCs, while in vivo treatment restored pulmonary CD4^{+}/CD8^{+} balance, attenuated lung injury, and improved survival in CLP-induced sepsis. This biomimetic platform supports further preclinical evaluation of developmentally engineered BVO-DCs for sepsis-associated immunosuppression.

List of abbreviations

2D: Two-dimensional

3D: Three-dimensional

7-AAD: 7-Aminoactinomycin D

ALI: Acute lung injury

ANOVA: Analysis of variance

BALF: Bronchoalveolar lavage fluid

BCA: Bicinchoninic acid

bFGF: Basic fibroblast growth factor

BM-DC: Bone marrow-derived dendritic cell

BMP4: Bone morphogenetic protein 4

BVO: Blood vessel organoid

BVO-DC: Blood vessel organoid-derived dendritic cell

CD40L: CD40 ligand

CHPC: Committed hematopoietic progenitor cell

CLP: Cecal ligation and puncture

CRISPR/Cas: Clustered regularly interspaced short palindromic repeats/CRISPR-associated protein

DAPI: 4′,6-Diamidino-2-phenylindole

DC: Dendritic cell

DMEM: Dulbecco's modified Eagle medium

EB: Embryoid body

EHT: Endothelial-to-hematopoietic transition

ELISA: Enzyme-linked immunosorbent assay

ESC: Embryonic stem cell

EV: Empty vector

FBS: Fetal bovine serum

Flt3L: Fms-like tyrosine kinase 3 ligand

GM-CSF: Granulocyte-macrophage colony-stimulating factor

GO: Gene Ontology

GSEA: Gene Set Enrichment Analysis

H&E: Hematoxylin and eosin

HEC: Hemogenic endothelial cell

HPC: Hematopoietic progenitor cell

HSPC: Hematopoietic stem and progenitor cell

HRP: Horseradish peroxidase

IL: Interleukin

IVIS: In vivo imaging system

LIF: Leukemia inhibitory factor

Lin: Lineage

LPS: Lipopolysaccharide

mESC: Mouse embryonic stem cell

MHC: Major histocompatibility complex

MHC-II: Major histocompatibility complex class II

MOI: Multiplicity of infection

MPO: Myeloperoxidase

NEAA: Non-essential amino acids

OVA: Ovalbumin

PBS: Phosphate-buffered saline

PCA: Principal component analysis

PD-1: Programmed cell death protein 1

PDGFR-β: Platelet-derived growth factor receptor beta

RIPA: Radioimmunoprecipitation assay

RPMI: Roswell Park Memorial Institute

RT-qPCR: Reverse transcription quantitative polymerase chain reaction

SCF: Stem cell factor

SD: Standard deviation

SDS-PAGE: Sodium dodecyl sulfate-polyacrylamide gel electrophoresis

TNF-α: Tumor necrosis factor alpha

TPO: Thrombopoietin

VEGF: Vascular endothelial growth factor

W/D: Wet-to-dry weight ratio

β-cat^{OE}: β-Catenin-overexpressing

Declarations

Ethics approval and consent to participate

All animal procedures were approved by the Institutional Animal Care and Use Committee of the Institute of Health and Medicine, Hefei Comprehensive National Science Center (approval no. IHM-AP-2025-093) and were performed in accordance with relevant institutional guidelines. Consent to participate was not applicable.

Consent for publication

Not applicable.

Availability of data and materials

The RNA-sequencing data are publicly available in the Zenodo repository at https://doi.org/10.5281/zenodo.21492677 [48]. All other data supporting the findings of this study are available within the article and its additional files or from the corresponding author upon reasonable request.

Competing interests

The authors declare that they have no competing interests.

Funding

This work was supported by the National Natural Science Foundation of China (Grant Nos. 82241050 to M.Z. and 82402511 to T.W.), the Anhui Provincial Health Project Fund (Grant No. AHWJ2024Aa40017 to M.Z.), the Clinical Medical Research Transformation Project of Anhui Province (Grant No. 202527c10020049 to M.Z.), the Doctoral Research Project of the Anhui Provincial Department of Education (Grant No. 2025AHGXZK50135 to J.S.), and the Joint Fund for New Medicine of USTC (Grant

No. YD9110002040 to D.W.).

Authors' contributions

D.W., X.C., and J.S. contributed equally to this work. D.W. performed the principal experimental work, analyzed the data, and wrote the original draft. X.C. and J.S. contributed to the design of the cell-based experiments and data analysis. T.W. contributed to the establishment and implementation of the CLP model. L.S. and F.X. contributed to DC differentiation and immunomagnetic enrichment. Q.W. contributed to the OVA-specific antigen-presentation and T-cell activation assays. X.F. and Q.M. contributed to transcriptomic profiling and bioinformatic analysis. Y.Z. and S.Y. provided methodological guidance and supervision for mESC culture and genetic engineering. M.Z. conceived and designed the study and supervised the overall project. All authors discussed and interpreted the results, reviewed the manuscript, and approved the final version.

Acknowledgements

The authors gratefully acknowledge the Center for Stem Cell and Translational Medicine, School of Life Sciences, Anhui University, for providing technical support.

Additional files

Additional file 1 (.pdf): Supplementary Figures S1–S9 and Tables S1–S5. This file contains supplementary experimental data, gating strategies, reagent information, primers, antibodies, and software details.

Additional file 2 (.pdf): Uncropped images of all western blots. This file contains the uncropped and unprocessed western blot images corresponding to the indicated figures.

REFERENCES

1. Evans L, Rhodes A, Alhazzani W, Antonelli M, Coopersmith CM, French C, et al. Surviving sepsis campaign: international guidelines for management of sepsis and septic shock 2021. Intensive Care Med. 2021;47:1181–247. doi:10.1007/s00134-021-06506-y.

2. Fujishima S, Gando S, Daizoh S, Kushimoto S, Ogura H, Mayumi T, et al. Infection site is predictive of outcome in acute lung injury associated with severe sepsis and septic shock. Respirology. 2016;21:898–904. doi:10.1111/resp.12769.

3. Zhang J, Yan W, Dong Y, Luo X, Miao H, Maimaijuma T, et al. Early identification and diagnosis, pathophysiology, and treatment of sepsis-related acute lung injury: a narrative review. J Thorac Dis. 2024;16:5457–76. doi:10.21037/jtd-24-1191.

4. Rubio I, Osuchowski MF, Shankar-Hari M, Skirecki T, Winkler MS, Lachmann G, et al. Current gaps in sepsis immunology: new opportunities for translational research. Lancet Infect Dis. 2019;19:e422–e436. doi:10.1016/S1473-3099(19)30567-5.

5. Leu S-W, Chu C-M, Chung C-J, Huang C-Y, Wang C-H, Li L-F, Wu H-P. Cell death of alveolar lymphocytes and monocytes is negatively correlated with driving pressure and mechanical power in patients with acute respiratory distress syndrome. Eur J Med Res. 2024;29:16. doi:10.1186/s40001-023-01607-4.

6. Rao D-X, Sun X-Y, Chen R. Analysis of pathogen spectrum in bronchoalveolar lavage fluid, T lymphocyte depletion, and prognosis in patients with severe pneumonia complicated by ARDS. Eur J Med Res. 2025;30:1229. doi:10.1186/s40001-025-03589-x.

7. Danahy DB, Anthony SM, Jensen IJ, Hartwig SM, Shan Q, Xue H-H, et al. Polymicrobial sepsis impairs bystander recruitment of effector cells to infected skin despite optimal sensing and alarming function of skin resident memory CD8 T cells. PLoS Pathog. 2017;13:e1006569. doi:10.1371/journal.ppat.1006569.

8. Zhang S, Mo S, Huang W, Zhong D, Yang X, Xie S, et al. Dendritic cell vaccines: Current research progress, challenges, and opportunities. Genes Dis. 2026;13:101913. doi:10.1016/j.gendis.2025.101913.

9. Heras-Murillo I, Mañanes D, Munné P, Núñez V, Herrera J, Catalá-Montoro M, et al. Immunotherapy with conventional type-1 dendritic cells induces immune memory and limits tumor relapse. Nat Commun. 2025;16:3369. doi:10.1038/s41467-025-58289-1.

10. Li R, Yi W, Qian X, Hu S, Shen H, Yan D, Li Y. Nanobiotechnology for dendritic cell-based cancer immunotherapy. Cell Biomaterials. 2026:100485. doi:10.1016/j.celbio.2026.100485.

11. Soldner F, Jaenisch R. Stem Cells, Genome Editing, and the Path to Translational Medicine. Cell. 2018;175:615–32. doi:10.1016/j.cell.2018.09.010.

12. Ge J-Y, Wang Y, Li Q-L, Liu F-K, Lei Q-K, Zheng Y-W. Trends and challenges in organoid modeling and expansion with pluripotent stem cells and somatic tissue. PeerJ. 2024;12:e18422. doi:10.7717/peerj.18422.

13. Shao Y, Fu J. Engineering multiscale structural orders for high-fidelity embryoids and organoids. Cell Stem Cell. 2022;29:722–43. doi:10.1016/j.stem.2022.04.003.

14. Ruiz-Herguido C, Guiu J, D'Altri T, Inglés-Esteve J, Dzierzak E, Espinosa L, Bigas A. Hematopoietic stem cell development requires transient Wnt/β-catenin activity. J Exp Med. 2012;209:1457–68. doi:10.1084/jem.20120225.

15. Carpenter KA, Thurlow KE, Craig SEL, Grainger S. Wnt regulation of hematopoietic stem cell development and disease. Curr Top Dev Biol. 2023;153:255–79. doi:10.1016/bs.ctdb.2022.12.001.

16. Jiang Z, Zhou W, Tian X, Zou P, Li N, Zhang C, et al. A Protective Role of Canonical Wnt/β-Catenin Pathway in Pathogenic Bacteria-Induced Inflammatory Responses. Mediators Inflamm. 2024;2024:8869510. doi:10.1155/2024/8869510.

17. Gatica-Andrades M, Vagenas D, Kling J, Nguyen TTK, Benham H, Thomas R, et al. WNT ligands contribute to the immune response during septic shock and amplify endotoxemia-driven inflammation in mice. Blood Advances. 2017;1:1274–86. doi:10.1182/bloodadvances.2017006163.

18. Suryawanshi A, Manoharan I, Hong Y, Swafford D, Majumdar T, Taketo MM, et al. Canonical wnt signaling in dendritic cells regulates Th1/Th17 responses and suppresses autoimmune neuroinflammation. J Immunol. 2015;194:3295–304. doi:10.4049/jimmunol.1402691.

19. Manicassamy S, Reizis B, Ravindran R, Nakaya H, Salazar-Gonzalez RM, Wang Y-C, Pulendran B. Activation of beta-catenin in dendritic cells regulates immunity versus tolerance in the intestine. Science. 2010;329:849–53. doi:10.1126/science.1188510.

20. Karnam A, Bonam SR, Rambabu N, Wong SSW, Aimanianda V, Bayry J. Wnt-β-Catenin Signaling in Human Dendritic Cells Mediates Regulatory T-Cell Responses to Fungi via the PD-L1 Pathway. mBio. 2021;12:e0282421. doi:10.1128/mBio.02824-21.

21. Wimmer RA, Leopoldi A, Aichinger M, Kerjaschki D, Penninger JM. Generation of blood vessel organoids from human pluripotent stem cells. Nat Protoc. 2019;14:3082–100. doi:10.1038/s41596-019-0213-z.

22. Love MI, Huber W, Anders S. Moderated estimation of fold change and dispersion for RNA-seq data with DESeq2. Genome Biol. 2014;15:550. doi:10.1186/s13059-014-0550-8.

23. Rittirsch D, Huber-Lang MS, Flierl MA, Ward PA. Immunodesign of experimental sepsis by cecal ligation and puncture. Nat Protoc. 2009;4:31–6. doi:10.1038/nprot.2008.214.

24. Ferguson LT, Rashied AA, Liang Z, Yumoto T, Anyalebechi JC, Swift DA, et al. A Novel Scoring System for Humane Endpoints in Mice with Cecal Ligation and Puncture-Induced Sepsis. Comp Med. 2023;73:446–60. doi:10.30802/AALAS-CM-22-000124.

25. Matute-Bello G, Downey G, Moore BB, Groshong SD, Matthay MA, Slutsky AS, Kuebler WM. An official American Thoracic Society workshop report: features and measurements of experimental acute lung injury in animals. Am J Respir Cell Mol Biol. 2011;44:725–38. doi:10.1165/rcmb.2009-0210ST.

26. Wimmer RA, Leopoldi A, Aichinger M, Wick N, Hantusch B, Novatchkova M, et al. Human blood vessel organoids as a model of diabetic vasculopathy. Nature. 2019;565:505–10. doi:10.1038/s41586-018-0858-8.

27. Nikolova MT, He Z, Seimiya M, Jonsson G, Cao W, Okuda R, et al. Fate and state transitions during human blood vessel organoid development. Cell. 2025;188:3329–3348.e31. doi:10.1016/j.cell.2025.03.037.

28. Salewskij K, Penninger JM. Blood Vessel Organoids for Development and Disease.

Circulation Research. 2023;132:498–510. doi:10.1161/CIRCRESAHA.122.321768.

29. Naderi-Meshkin H, Cornelius VA, Eleftheriadou M, Potel KN, Setyaningsih WAW, Margariti A. Vascular organoids: unveiling advantages, applications, challenges, and disease modelling strategies. Stem Cell Research & Therapy. 2023;14:292. doi:10.1186/s13287-023-03521-2.

30. Ottersbach K. Endothelial-to-haematopoietic transition: an update on the process of making blood. Biochem Soc Trans. 2019;47:591–601. doi:10.1042/BST20180320.

31. Montel-Hagen A, Seet CS, Li S, Chick B, Zhu Y, Chang P, et al. Organoid-Induced Differentiation of Conventional T Cells from Human Pluripotent Stem Cells. Cell Stem Cell. 2019;24:376-389.e8. doi:10.1016/j.stem.2018.12.011.

32. Nafria M, Bonifer C, Stanley EG, Ng ES, Elefanty AG. Protocol for the Generation of Definitive Hematopoietic Progenitors from Human Pluripotent Stem Cells. STAR Protoc. 2020;1:100130. doi:10.1016/j.xpro.2020.100130.

33. Sturgeon CM, Ditadi A, Awong G, Kennedy M, Keller G. Wnt signaling controls the specification of definitive and primitive hematopoiesis from human pluripotent stem cells. Nat Biotechnol. 2014;32:554–61. doi:10.1038/nbt.2915.

34. Liu J, Xiao Q, Xiao J, Niu C, Li Y, Zhang X, et al. Wnt/β-catenin signalling: function, biological mechanisms, and therapeutic opportunities. Signal Transduct Target Ther. 2022;7:3. doi:10.1038/s41392-021-00762-6.

35. Ying Q-L, Wray J, Nichols J, Batlle-Morera L, Doble B, Woodgett J, et al. The ground state of embryonic stem cell self-renewal. Nature. 2008;453:519–23. doi:10.1038/nature06968.

36. Swafford D, Manicassamy S. Wnt signaling in dendritic cells: its role in regulation of immunity and tolerance. Discov Med. 2015;19:303–10.

37. Fu C, Liang X, Cui W, Ober-Blöbaum JL, Vazzana J, Shrikant PA, et al. β-Catenin in dendritic cells exerts opposite functions in cross-priming and maintenance of CD8+ T cells through regulation of IL-10. Proc Natl Acad Sci U S A. 2015;112:2823–8. doi:10.1073/pnas.1414167112.

38. Fu C, Wang J, Ma T, Yin C, Zhou L, Clausen BE, et al. β-Catenin in Dendritic Cells Negatively Regulates CD8 T Cell Immune Responses through the Immune Checkpoint Molecule Tim-3. Vaccines (Basel). 2024;12:460. doi:10.3390/vaccines12050460.

39. Jost M, Jacobson AN, Hussmann JA, Cirolia G, Fischbach MA, Weissman JS. CRISPR-based functional genomics in human dendritic cells. Elife. 2021;10:e65856. doi:10.7554/eLife.65856.

40. Prakash M, Cortez CD, Jayaraman A, Hsu S-Y, Huang Y-C, Yeh C-Y, Lee YL. Innovative gene engineering and drug delivery systems for dendritic cells in cancer immunotherapy. J Biomed Sci. 2025;32:95. doi:10.1186/s12929-025-01191-1.

41. Awasthi S, Singh B, Welliver RC, Dietert RR. Lung dendritic cell developmental programming, environmental stimuli, and asthma in early periods of life. J Allergy (Cairo). 2012;2012:176468. doi:10.1155/2012/176468.

42. Zhang S, Audiger C, Chopin M, Nutt SL. Transcriptional regulation of dendritic

cell development and function. Front Immunol. 2023;14:1182553. doi:10.3389/fimmu.2023.1182553.

43. Møller SH, Wang L, Ho P-C. Metabolic programming in dendritic cells tailors immune responses and homeostasis. Cell Mol Immunol. 2022;19:370–83. doi:10.1038/s41423-021-00753-1.

44. Wherry EJ, Kurachi M. Molecular and cellular insights into T cell exhaustion. Nat Rev Immunol. 2015;15:486–99. doi:10.1038/nri3862.

45. Zhang Y, Li J, Lou J, Zhou Y, Bo L, Zhu J, et al. Upregulation of programmed death-1 on T cells and programmed death ligand-1 on monocytes in septic shock patients. Crit Care. 2011;15:R70. doi:10.1186/cc10059.

46. Boomer JS, To K, Chang KC, Takasu O, Osborne DF, Walton AH, et al. Immunosuppression in patients who die of sepsis and multiple organ failure. JAMA. 2011;306:2594–605. doi:10.1001/jama.2011.1829.

47. Hotchkiss RS, Monneret G, Payen D. Sepsis-induced immunosuppression: from cellular dysfunctions to immunotherapy. Nat Rev Immunol. 2013;13:862–74. doi:10.1038/nri3552.

48. Wang D. Organoid-derived β-catenin-overexpressing dendritic cells alleviate sepsis-induced acute lung injury. Zenodo. 2026. https://doi.org/10.5281/zenodo.21492677.

Figure Legends

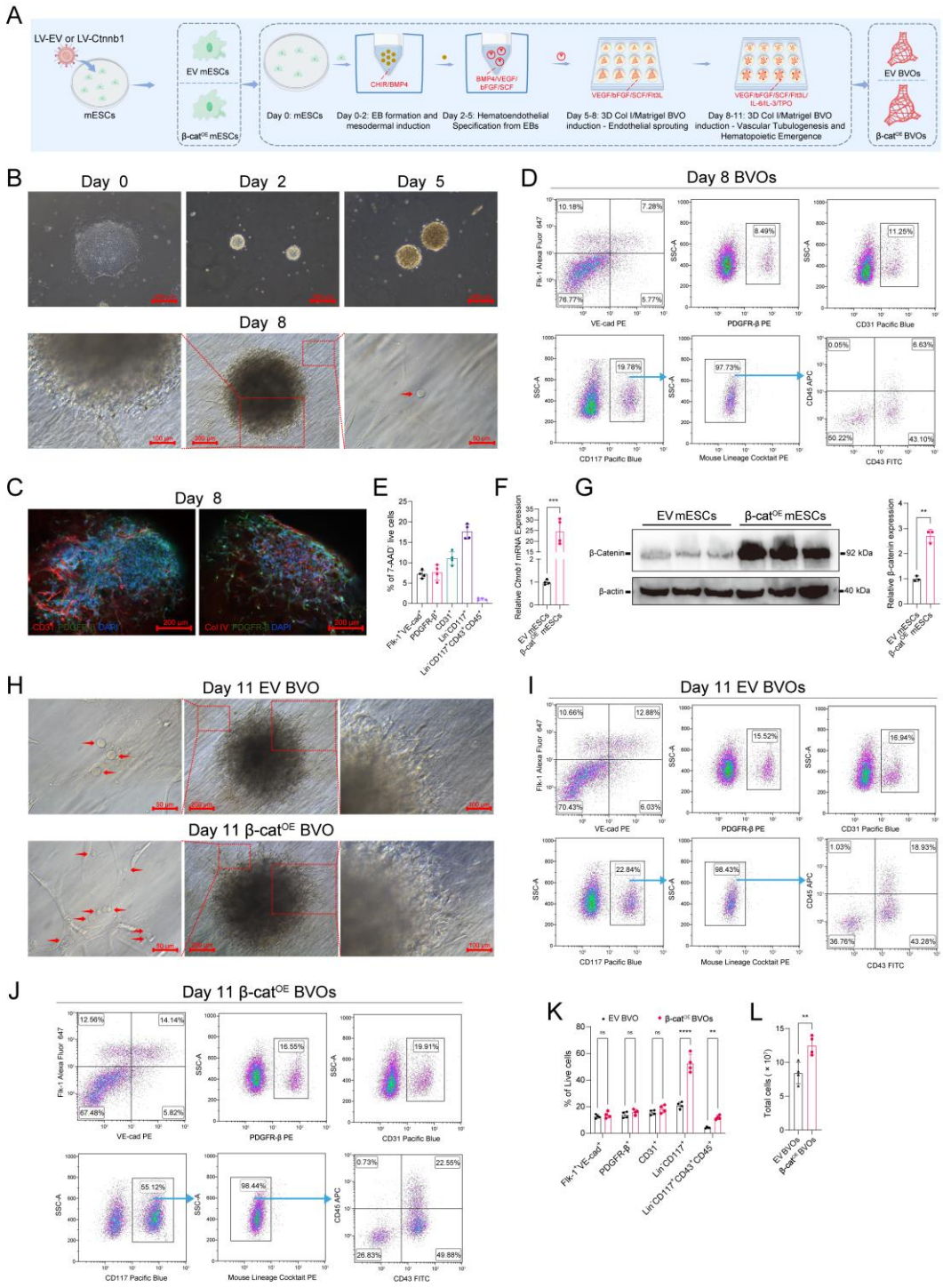


Figure 1. β-Catenin overexpression enhances hematopoietic progenitor generation during blood vessel organoid differentiation.

A) Generation of empty-vector (EV) and β-catenin-overexpressing (β-cat^{OE}) blood vessel organoids (BVOs) from mouse embryonic stem cells (mESCs): embryoid body formation and mesodermal induction (Days 0–2), hematoendothelial specification

(Days 2–5), endothelial sprouting (Days 5–8), and vascular tubulogenesis with hematopoietic emergence (Days 8–11). B) Phase-contrast images of BVO development. Red arrows indicate phase-bright hematopoietic-like cells. Scale bars: 200 μm (Days 0, 2, and 5) and 100, 200, and 50 μm (Day 8, left to right). C) Whole-mount confocal images of Day 8 BVOs stained for CD31 (red), PDGFR-β (green), collagen IV (Col IV; red), and DAPI (blue). Scale bars, 200 μm. D) Flow-cytometric identification of Flk-1^{+}VE-$cadherin^{+}$ hemogenic endothelial cells, PDGFR-β^{+} perivascular cells, $CD31^{+}$ endothelial cells, and $CD117^{+}Lin^{-}CD43^{+}CD45^{+}$ hematopoietic progenitor cells (HPCs) in Day 8 BVOs. E) Frequencies of the indicated populations among 7-AAD^{-} live cells in Day 8 BVOs (n = 4). F) RT-qPCR analysis of Ctnnb1 expression in EV and β-cat^{OE} mESCs (n = 4). G) Western blot and densitometric analysis of β-catenin in EV and β-cat^{OE} mESCs; β-actin was the loading control (n = 3). H) Phase-contrast images of Day 11 EV and β-cat^{OE} BVOs. Red arrows indicate hematopoietic-like cells. Scale bars: 50, 200, and 100 μm (left to right). I,J) Flow-cytometric identification of hemogenic endothelial, perivascular, endothelial, and hematopoietic populations in Day 11 BVOs. K) Frequencies of the indicated populations among 7-AAD^{-} live cells (n = 4). L) Total Day 11 cell yields (n = 4). For E–G and K,L, n denotes independent biological replicates. Data are mean ± SD. Two-group comparisons used two-tailed Student's t-tests; cell type × BVO group comparisons used two-way ANOVA with Šídák's multiple-comparisons test. ns, not significant; **P < 0.01; ***P < 0.001; ****P < 0.0001.

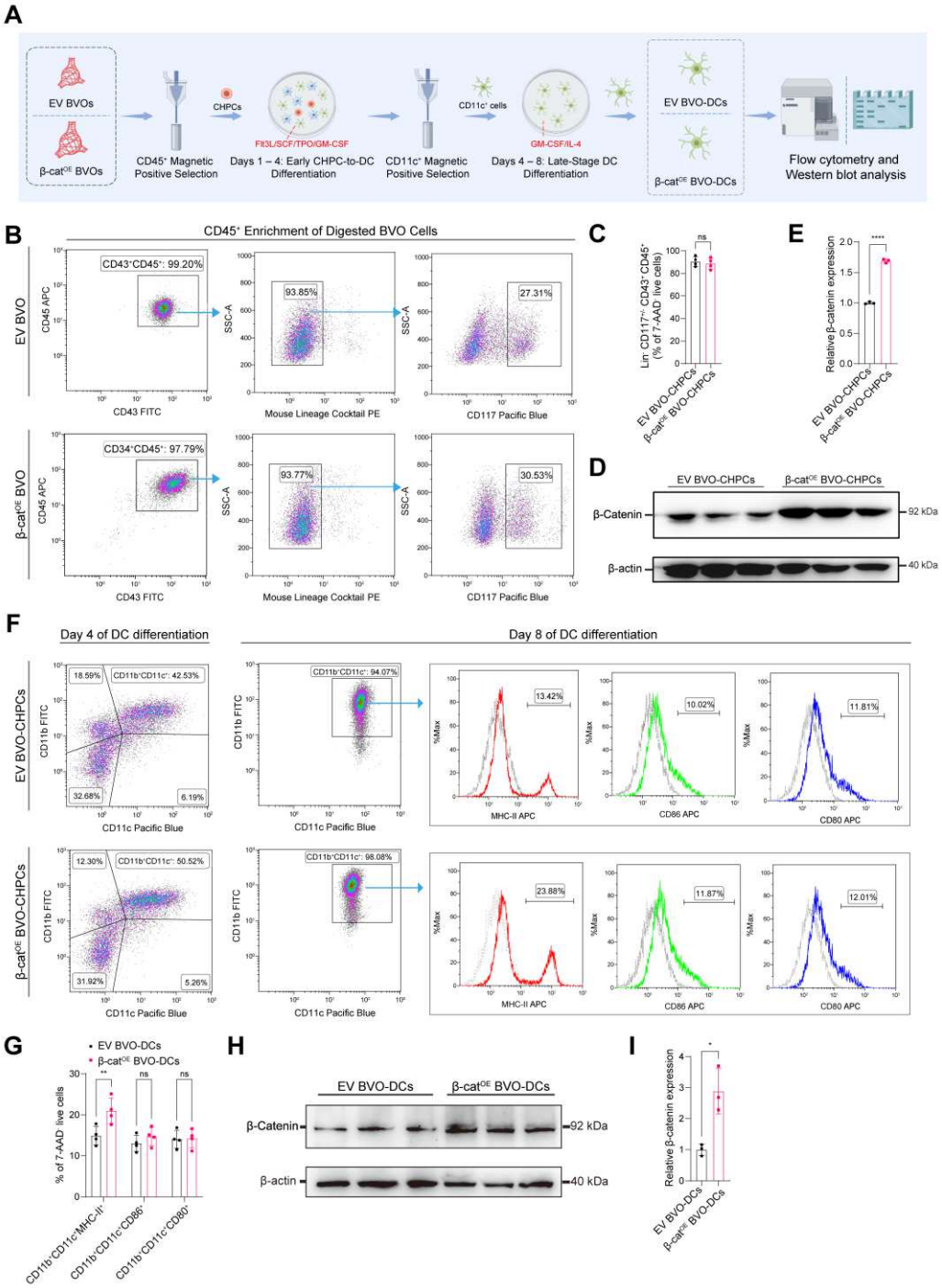
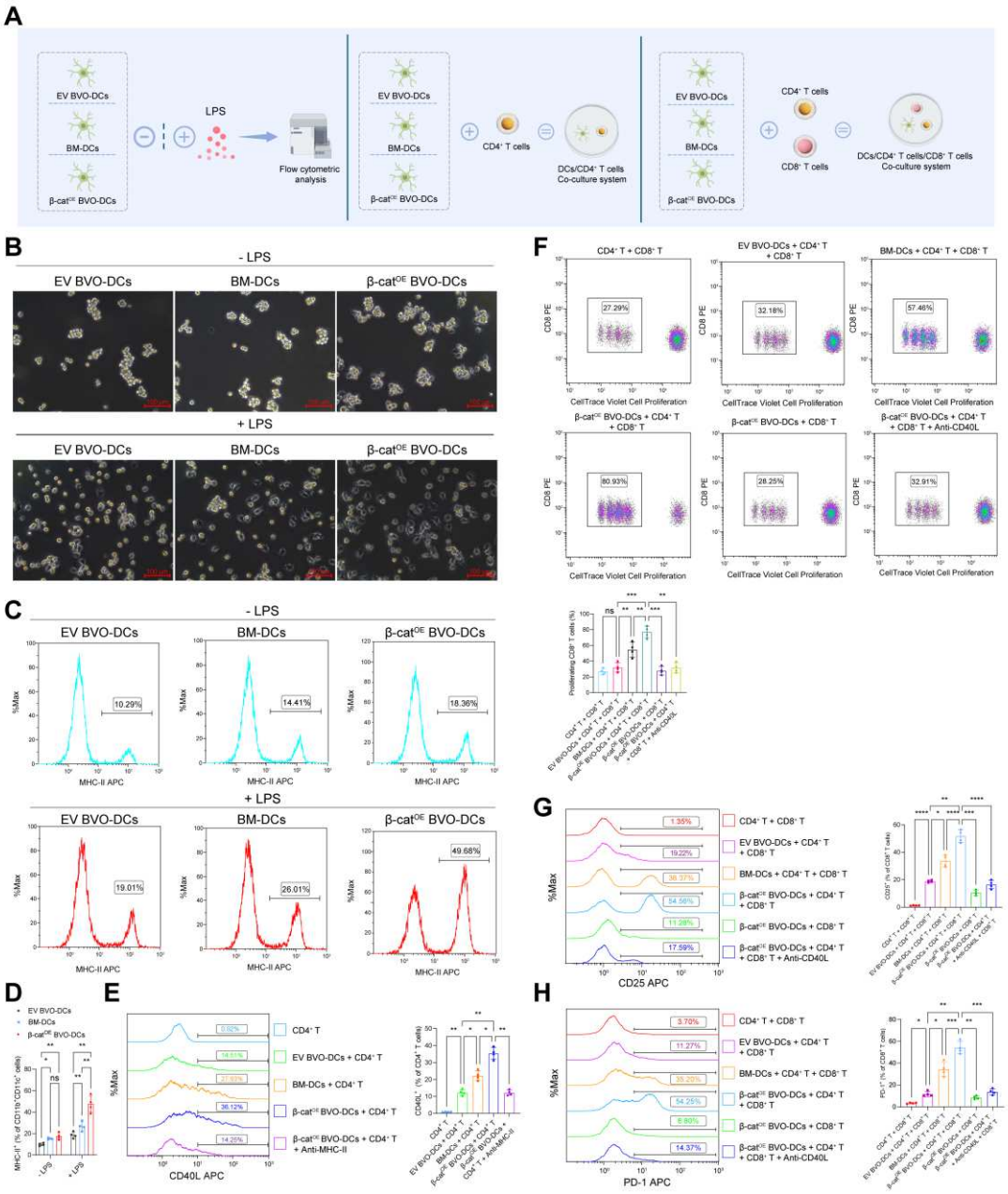


Figure 2. Stepwise generation and phenotypic characterization of EV and β-cat^{OE} BVO-derived dendritic cells.

A) Schematic of positive immunomagnetic enrichment of CD45^{+} hematopoietic cells from dissociated EV and β-cat^{OE} BVOs, followed by early (Days 1–4) and late-stage (Days 4–8) dendritic cell (DC) differentiation and flow-cytometric and Western blot analyses. B) Representative flow-cytometric characterization of CD45-enriched cells

from EV and β-cat^{OE} BVOs, showing sequential identification of CD43^{+}CD45^{+}, lineage-negative (Lin^{-}), and CD117^{+} and CD117^{-} fractions. The resulting Lin^{-}CD43^{+}CD45^{+} population containing both CD117^{+} and CD117^{-} cells was operationally designated the committed hematopoietic progenitor cell (CHPC)-enriched population. C) Quantification of Lin^{-}CD117$^{+/-}$CD43^{+}CD45^{+} cells relative to the total 7-AAD^{-} live-cell population (n = 4 independent biological replicates). D and E) Western blot and densitometric analysis of β-catenin expression in EV and β-cat^{OE} BVO-CHPCs; β-actin served as the loading control (n = 3 independent biological replicates). F) Representative flow-cytometric profiles of CD11b and CD11c expression on Day 4 and of CD11b, CD11c, MHC-II, CD86, and CD80 expression following CD11c^{+} enrichment and late-stage differentiation on Day 8. G) Quantification of CD11b^{+}CD11c^{+}MHC-II^{+}, CD11b^{+}CD11c^{+}CD86^{+}, and CD11b^{+}CD11c^{+}CD80^{+} cells relative to the total 7-AAD^{-} live-cell population on Day 8 (n = 4 independent biological replicates). H, I) Western blot and densitometric analysis of β-catenin expression in Day 8 EV and β-cat^{OE} BVO-derived DCs; β-actin served as the loading control (n = 3 independent biological replicates). Data are presented as mean ± SD. Two-group comparisons were performed using two-tailed Student's t-tests, and comparisons involving marker and BVO group were performed using two-way ANOVA with Šídák's multiple-comparisons test. ns, not significant; *P < 0.05; **P < 0.01; ****P < 0.0001.



1276 **Figure 3. β-cat^{OE} BVO-DCs enhance OVA-specific T-cell proliferation and**
1277 **activation through the MHC-II/CD4$^+$ T-cell/CD40L axis.**

1278 A) Schematic of LPS-induced dendritic cell (DC) maturation, DC/OT-II CD4$^+$ T-cell
1279 co-culture, and DC/OT-II CD4$^+$/OT-I CD8$^+$ T-cell tri-culture assays using full-length
1280 ovalbumin (OVA). B) Representative phase-contrast images of EV BVO-DCs, primary
1281 bone marrow-derived DCs (BM-DCs), and β-cat^{OE} BVO-DCs cultured with or without
1282 LPS for 48 h. Scale bars, 100 μm. C) Representative MHC-II histograms within the 7-
1283 AAD$^-$CD11b$^+$CD11c$^+$ population under −LPS and +LPS conditions. D) Frequencies of
1284 MHC-II$^+$ cells within the CD11b$^+$CD11c$^+$ population (n = 4 matched independent

experiments). E) Representative histograms and frequencies of $CD40L^+$ cells among 7-$AAD^-CD3^+CD4^+$ OT-II T cells cultured without DCs or with the indicated DCs and full-length OVA, including MHC-II blockade. The upstream gating strategy is shown in Additional file 1: Figure S8 (n = 4 matched independent experiments). F) Representative plots and frequencies of proliferating CellTrace Violet-low 7-$AAD^-CD4^-CD8^+$ OT-I cells in the indicated full-length OVA-containing tri-cultures, including $CD4^+$ T-cell omission and CD40L blockade. The upstream gating strategy is shown in Additional file 1: Figure S9A (n = 4 matched independent experiments). G,H) Representative histograms and frequencies of $CD25^+$ (G) and $PD\text{-}1^+$ (H) cells within the gated OT-I population. CD25 and PD-1 were measured in separate staining tubes using parallel tri-cultures without CellTrace Violet; the upstream gating strategy is shown in Additional file 1: Figure S9B (n = 4 matched independent experiments). Short-term PD-1 upregulation was interpreted as activation-associated checkpoint induction rather than T-cell exhaustion. Data are mean ± SD. Panel D was analyzed by two-way repeated-measures ANOVA with Tukey's multiple-comparisons test. Panels E–H were analyzed by one-way repeated-measures ANOVA with Geisser–Greenhouse correction and Tukey's multiple-comparisons test. ns, not significant; *P < 0.05; **P < 0.01; ***P < 0.001; ****P < 0.0001.

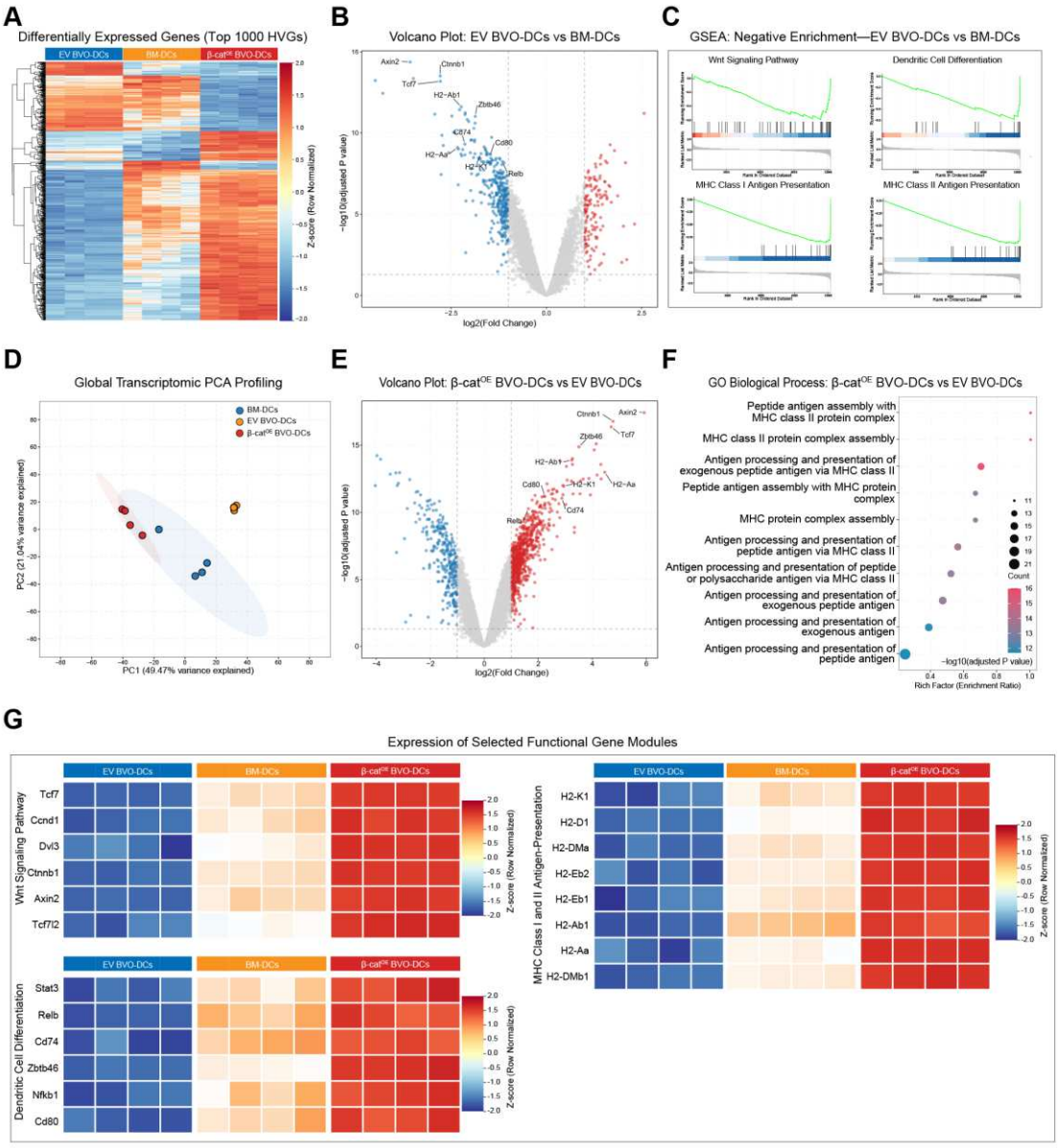


Figure 4. β-Catenin overexpression reprograms BVO-DCs toward dendritic cell differentiation and antigen-presentation-associated transcriptional states.

A) Unsupervised hierarchical clustering heatmap of the 1,000 most highly variable genes in EV BVO-DCs, primary BM-DCs, and β-cat^{OE} BVO-DCs. Expression values were variance-stabilized and standardized to row-wise Z-scores. B) Volcano plot showing differentially expressed genes in EV BVO-DCs relative to BM-DCs. C) Gene Set Enrichment Analysis (GSEA) showing negative enrichment of the Wnt signaling, dendritic cell differentiation, MHC class I antigen-presentation, and MHC class II antigen-presentation gene sets in EV BVO-DCs relative to BM-DCs. D) Principal

component analysis of the global transcriptomic profiles. Shaded ellipses indicate the distribution of samples within each group. E) Volcano plot showing differentially expressed genes in β-cat^{OE} BVO-DCs relative to EV BVO-DCs. In B and E, red and blue indicate significantly upregulated and downregulated genes, respectively, whereas gray indicates genes that did not meet the differential-expression thresholds. Differentially expressed genes were defined by an adjusted P value < 0.05 and $|\log_2$ fold change$| \geq 1$. F) Gene Ontology Biological Process enrichment analysis of genes significantly upregulated in β-cat^{OE} BVO-DCs relative to EV BVO-DCs. Bubble size represents gene count, the horizontal axis represents rich factor, and color represents $-\log_{10}$-adjusted P value. G) Row-wise Z-score-normalized heatmaps showing selected genes associated with Wnt signaling, dendritic cell differentiation, and MHC class I and II antigen presentation. Four independently prepared biological replicates were analyzed per group. Differential-expression testing was performed using DESeq2 with the Wald test, and P values were adjusted using the Benjamini–Hochberg method. GSEA and Gene Ontology enrichment P values were also adjusted using the Benjamini–Hochberg method. HVG, highly variable gene; PCA, principal component analysis; GO, Gene Ontology.

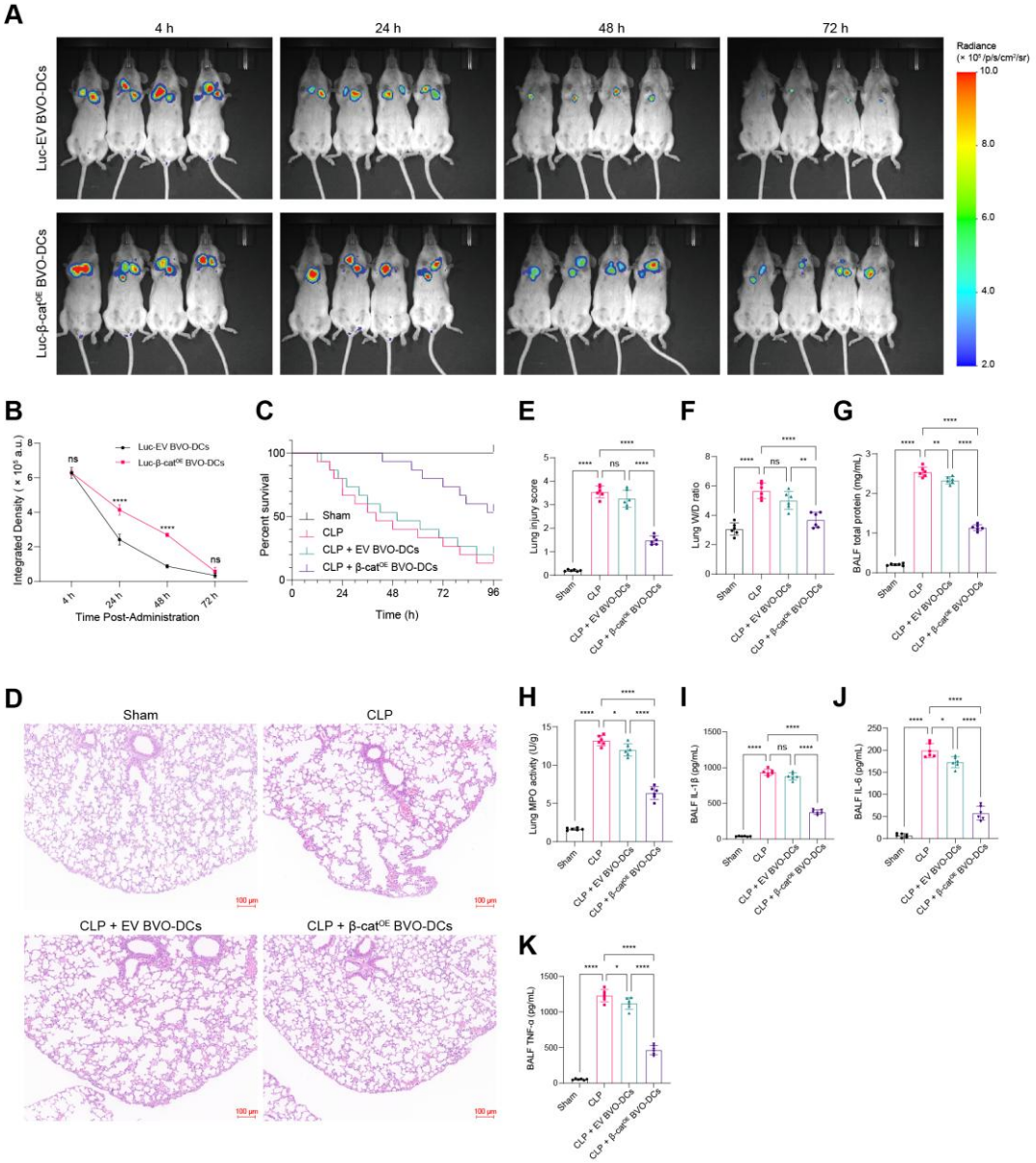


Figure 5. β-cat^{OE} BVO-DC treatment improves survival and attenuates CLP-induced acute lung injury and pulmonary inflammation.

A) Representative in vivo bioluminescence images of mice receiving intranasal luciferase-expressing EV BVO-DCs (Luc-EV BVO-DCs) or β-cat^{OE} BVO-DCs (Luc-β-cat^{OE} BVO-DCs) at 4, 24, 48, or 72 h after administration. Independent cohorts were imaged at each time point (n = 4 mice per group per time point). The pseudocolor scale represents radiance. B) Fiji-derived integrated density of thoracic bioluminescence signals. Values were divided by 10^5 for graphical presentation and are expressed in arbitrary units (a.u.). Data were analyzed using ordinary two-way ANOVA followed by

Šídák's multiple-comparisons test. C) Kaplan–Meier survival curves of Sham, CLP, CLP + EV BVO-DC, and CLP + β-cat^{OE} BVO-DC groups monitored for 96 h (n = 15 mice per group). Survival curves were compared using the log-rank (Mantel–Cox) test with Bonferroni adjustment for pairwise comparisons. D) Representative hematoxylin and eosin-stained lung sections collected 48 h after CLP or sham surgery. Scale bars, 100 μm. E) Histopathological lung injury scores. F) Lung wet-to-dry weight ratios. G) Total protein concentrations in bronchoalveolar lavage fluid (BALF). H) Lung myeloperoxidase (MPO) activity. I–K) BALF concentrations of IL-1β (I), IL-6 (J), and TNF-α (K). For D–K, n = 5 mice per group. Histopathological scoring was performed in a blinded manner across multiple fields for each animal, with the animal-level mean used as one biological replicate. Data are presented as mean ± SD. Panels E–K were analyzed using one-way ANOVA followed by Tukey's multiple-comparisons test. ns, not significant; *P < 0.05; **P < 0.01; ****P < 0.0001. CLP, cecal ligation and puncture.

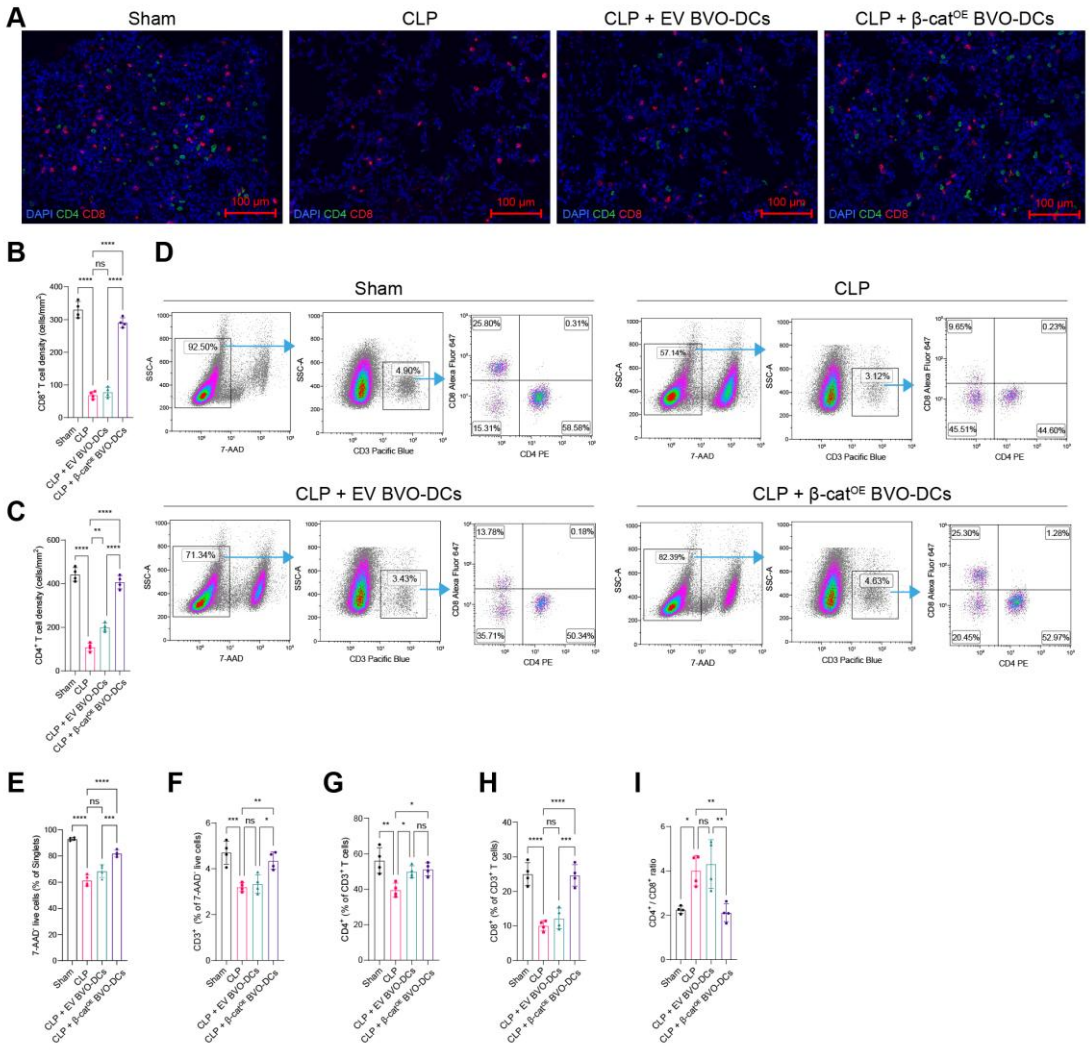


Figure 6. β-cat^{OE} BVO-DC treatment restores pulmonary T-cell abundance and CD4$^+$/CD8$^+$ balance in CLP-induced lung injury.

A) Representative multiplex immunofluorescence confocal images of lung sections collected 48 h after CLP or sham surgery. DAPI, blue; CD4, green; CD8, red. Scale bars, 100 μm. B,C) Quantification of CD8$^+$ (B) and CD4$^+$ (C) T-cell densities (n = 5 mice per group). Three non-consecutive lung sections were examined per animal, with five randomly selected, non-overlapping fields analyzed per section. Measurements from the 15 fields were averaged to obtain a single biological value for each animal. D) Representative flow-cytometric gating strategy for bronchoalveolar lavage fluid (BALF)-derived cells. Singlets were sequentially gated as 7-AAD$^-$ live cells and CD3$^+$ T cells, after which CD4$^+$ and CD8$^+$ subsets were resolved within the CD3$^+$ population. E) Frequency of 7-AAD$^-$ live cells among singlets. F) Frequency of CD3$^+$ T cells within

the 7-AAD⁻ live-cell gate. G,H) Frequencies of CD4⁺ (G) and CD8⁺ (H) T cells within the CD3⁺ population. I) CD4⁺/CD8⁺ ratio, calculated separately for each mouse from the corresponding CD4⁺ and CD8⁺ frequencies before group-level analysis. For E–I, n = 4 mice per group. Data are presented as mean ± SD and were analyzed using one-way ANOVA followed by Tukey's multiple-comparisons test. ns, not significant; *P < 0.05; **P < 0.01; ***P < 0.001; ****P < 0.0001. BALF, bronchoalveolar lavage fluid; CLP, cecal ligation and puncture.

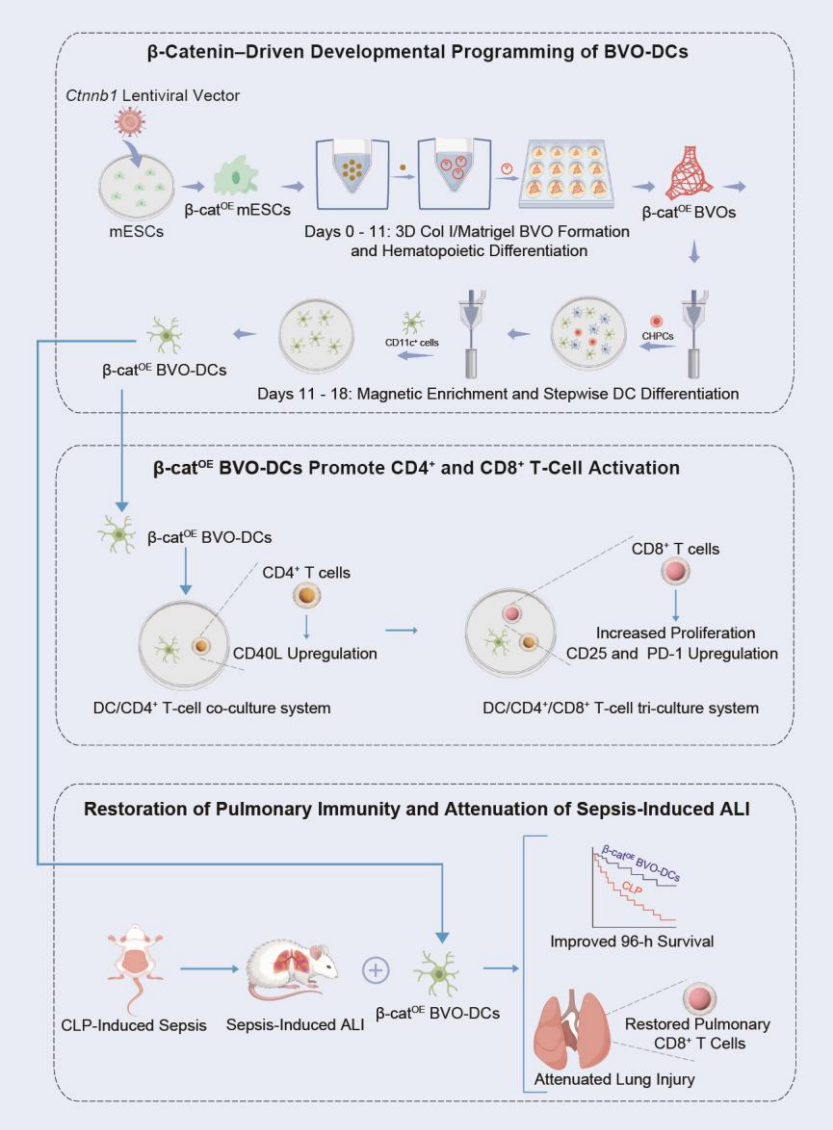


Figure 7. Schematic of β-catenin-driven BVO-DC development and immune restoration in sepsis-induced acute lung injury.

β-Catenin-overexpressing mESCs were sequentially differentiated through BVO and CHPC stages into BVO-derived DCs. The resulting β-cat^{OE} BVO-DCs enhanced CD4⁺ T-cell CD40L expression and CD8⁺ T-cell proliferation and activation-associated

phenotypes in vitro. Following intranasal administration, β-cat^{OE} BVO-DC treatment was associated with increased pulmonary $CD8^+$ T-cell abundance, attenuated lung injury, and improved survival in CLP-induced sepsis.

Supplementary Files

This is a list of supplementary files associated with this preprint. Click to download.

- Additionalfile1SupplementaryFiguresS1S9andTablesS1S5.pdf
- Additionalfile2Uncroppedimagesofallwesternblots.pdf